JACS
JOURNAL OF THE AMERICAN CHEMICAL SOCIETY
pubs.acs.org/JACS
Article



# Probing Terra Incognita of Ni–P Catalysts: *Operando* Explorations during Hydrogen Evolution Reaction

Seongyoung Kong, Ernesto Soto, Jiyun Hong, Ryan Davis, Erik Nelson, Vladimir Roddatis, Oleg I. Lebedev, Weiran Zheng, Humphrey W. Odhiambo, Nakyung Oh, Vivek Upadhyay, Natalia C. M. Spera, Dhruv Raturi, Prashant Singh, Gaoyuan Ouyang, Fernando D. Vila, Simon R. Bare, Yury V. Kolen'ko, Duane D. Johnson, and Kirill Kovnir*

Cite This: *J. Am. Chem. Soc.* 2026, 148, 10241–10256

Read Online

ACCESS | Metrics & More | Article Recommendations | Supporting Information

**ABSTRACT:** We have developed two Ni phosphide preparation methods allowing *operando* XAS surface-sensitive studies of well-defined bulk systems. For Ni *K*-edge XAS, a $Ni_2P$ phase-pure powder was sintered into a high-density pellet and polished for grazing incidence XAS. Ni sites were mildly affected by the acidic electrolyte prior to the HER, while the applied cathodic potential caused the reduction of Ni surface states beyond the states of as-prepared $Ni_2P$. The computed fully H-covered $Ni_2P$ [0001] model describes the difference in the *operando* Ni *K*-edge GIXAS spectrum well. Upon turning the applied bias off, the Ni sites became immediately oxidized, forming NiO on the surface. Thus, the active phase during the HER is covalent $Ni^0$ close to that in the intermetallic phosphides, and $Ni^{2+}$ oxides formed after, and not during, the HER. For P *K*-edge XAS, Ni foam was phosphorized to form a thin $Ni_3P$ layer while preserving its high surface area. Upon immersion in the acidic electrolyte, the P sites underwent removal of $P^{5+}$ phosphates and formed new P coordination, possibly due to the adsorption of protons from the electrolyte. These new P surface states were not affected by turning the cathodic current on and off as soon as the sample was immersed in the acidic electrolyte. However, the removal of the sample from the electrochemical cell and drying in air resulted in substantial depletion and oxidation of surface P. Echoing the observed Ni site chemistry during HER, XAS and XPS suggest that the *in situ* active P sites are different from the oxidized P states observed under *ex situ* conditions.

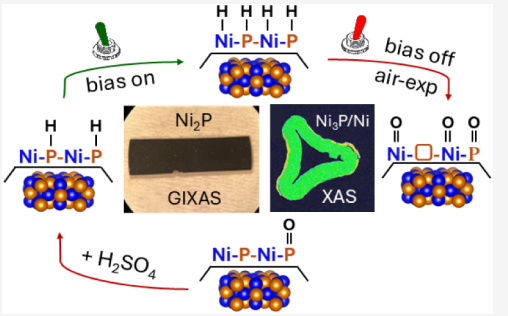


## INTRODUCTION

Hydrogen evolution reaction (HER) is an environmentally benign route to obtain hydrogen because it does not emit carbon byproducts, as opposed to the conventional reforming process of fossil fuels, which accounts for around 95% of global hydrogen production.[1] It is essential to develop efficient and abundant HER catalysts to realize a sustainable energy economy.[2] Platinum group metals (PGMs) are the most efficient HER catalysts, but their limited resources preclude large-scale production. Instead, there have been numerous research efforts to develop earth-abundant HER catalysts such as transition metal borides, carbides, nitrides, oxyhydroxides, chalcogenides, and phosphides, but there are still many remaining stages to reach the activity and durability of PGM catalysts.[3−6] To further improve the catalyst's performance, it is crucial to understand the behavior of active sites at the fundamental level.

Probing the active sites during electrocatalytic reactions requires a sophisticated experimental setup, as it needs to satisfy surface sensitivity as well as measurable conditions in the presence of a liquid electrolyte. Nevertheless, there have recently been significant advances in *operando* techniques, including X-ray diffraction (XRD), Raman, infrared (IR), X-ray absorption (XAS), and photoelectron (XPS) spectroscopies, as well as transmission electron microscopy (TEM), which commonly require ultrahigh vacuum.[7−17] In particular, XAS is a powerful tool since it is sensitive to the changes in the electronic structure [X-ray absorption near-edge spectra (XANES)] of probed elements and also provides information on local bonding environments [extended X-ray absorption fine structure (EXAFS)]. In electrocatalytic applications using high external bias, namely $CO_2$ reduction reaction ($CO_2$RR) or oxygen evolution reaction (OER), XAS effectively discloses the behavior of active sites that are not detected in *ex situ* conditions. The Yang group showed that the Cu species are largely reduced to metallic Cu nanograins as $CO_2$RR active

Received: January 24, 2026
Revised: February 12, 2026
Accepted: February 13, 2026
Published: February 24, 2026







https://doi.org/10.1021/jacs.6c01756
*J. Am. Chem. Soc.* 2026, 148, 10241−10256

sites.[18−20] On the other hand, active sites, such as Co or Ni, are generally oxidized during OER.[21−23] However, in the case of HER, the spectral changes are not as detectable, possibly due to the relatively low applied potential and higher surface stability under HER conditions. Nevertheless, some reports show the opposite oxidation state changes in the same element.[24−29] This indicates that *operando* XAS studies for HER are delicate and sensitive experiments, and there are other possible contributors that affect the behavior of the catalytically active sites. Thus, synergistic development of well-defined model samples and specific measurement conditions are needed to fully understand the catalysts.

Transition metal phosphides (*TMPs*) are one of the HER alternative catalysts to PGMs, and their versatile compositions draw the attention of researchers to explore potent catalytic performance among them.[30] $Ni_2P$ was the first predicted *TMP* HER catalyst due to its high hydrodesulfurization (HDS) activity, where the same active sites were expected to work effectively for HER.[31,32] $Ni_3P$ catalyst was later reported to be more active than $Ni_2P$ because $Ni_4P_4$ surface terminations undergo effective surface reconstructions upon applied bias.[33] Although calculations predict that $Ni_2P$ has strong H adsorption sites, such as hollow $Ni_3$, there has not been any direct observation of Ni surface states' journey during HER in that structure.[32−35] Moreover, the observation of the oxidized surface of Ni−P catalysts after HER often leads to confusion about whether oxidized species are active sites during HER.[30,36] The Lewis group reported a CoP thin-film case in acidic media, where oxide phases on the surface were reduced to metallic Co during HER, indicating that the active sites in *TMP* may experience reduction under the reductive potential of HER.[37] Thin-film-based samples composed of complex multilayered core−shell heterostructures may impede accurate resolution of the structural information. Such analysis can be reliably achieved through data-fusion approaches combining a full set of electron microscopy analyses (STEM, EELS, and EDX).[38] For other catalyst types, such as $MoS_2$, it was shown that Ni or Co dopants act as the main active sites, and their oxidation states were reduced during HER, whereas Mo stayed intact.[39,40] To probe the actual behavior of the Ni sites in Ni−P catalysts during HER, *operando* studies are necessary. In addition, there are scarce reports of the P site behavior during HER due to the relatively low energy of the P *K*-edge, 2.1 keV.[37] To elucidate the complete picture of catalytically active sites, it is important to probe both elements.

The sample preparation crucially affects the results of *operando* XAS studies. Three general sample preparation methods are all bottom-up approaches, including nanoparticle synthesis, thin film (electro)deposition, and chemical single-atom deposition to achieve high surface-to-bulk ratios.[35,39−44] These methods provide high surface sensitivity and circumvent self-absorption effects but exclude many catalysts that would have to be prepared via other synthetic routes. Especially, well-ordered bulk crystalline materials prepared by solid-state routes are omitted. Therefore, more universal methods for sample preparation need to be addressed. In this study, we have introduced new Ni−P sample preparation methods for *operando* XAS experiments. For the Ni *K*-edge sample, a top-down approach was applied. The sample was prepared by polishing the highly dense pellet pressed from a phase-pure $Ni_2P$ bulk powder. Since the prepared $Ni_2P$ sample is a bulk material, we have applied grazing incidence XAS (GIXAS) to inspect the surface as shallow as possible. Because of the limitations of polishing methods, surface roughness (≈12 nm) has hindered the ideal total reflection. Nevertheless, we have observed clear signals from electronic changes of surface Ni during HER. For the P *K*-edge sample, surface phosphorization was applied to Ni foam to form thin layers of $Ni_3P$ phosphide with high surface area. Despite the relatively thick phosphide layer and the low energy of the P *K*-edge, electronic structure changes of P sites during HER have also been observed. This study demonstrates the sample preparation approaches suitable for other solid-state materials, making *operando* XAS available beyond thin films/nanoparticles/atomically dispersed samples. As several terms referring to the condition of catalysts are used in this study, we denote the three states of the catalyst as follows: (*i*) *ex situ* − as-synthesized sample in air condition, (*ii*) *in situ* − sample in electrolyte without applied potential (or open circuit potential: OCP), and (*iii*) *operando* − sample in electrolyte and with applied potential. Our *operando* results provide an overall picture of Ni and P behavior in Ni−P HER catalysts, demonstrating that the *operando* HER active sites are not oxidized during HER. The surface oxidation of Ni sites occurs *ex situ* only after the reducing bias is turned off.

## EXPERIMENTAL SECTION

Warning: At high temperatures, e.g., 800 °C, excessive vapor pressure of P may compromise the silica ampules, resulting in shattering or explosion. The annealing steps must be conducted in a well-ventilated environment, such as in a fume hood. Placing the ampule into a preheated furnace is a hazardous procedure because the sudden rise in temperature, and the corresponding pressure of volatile P, may over-pressurize the ampule, leading to shattering. The amounts of sample in such experiments should be minimized, and excessive protection measures are required—face shield, thermal-resistant gloves, lab coats, and long tongs at a very minimum.

### $Ni_2P$ Synthesis

Elemental Ni powder (99.995%, Alfa Aesar) and red phosphorus powder (98.7%, Alfa Aesar) were used for the solid-state synthesis of $Ni_2P$ while CsCl (99.8%, Alfa Aesar) was used as a salt flux. A mixture of 2:1.03 Ni:P with a total weight of 0.3 g was loaded into the glassy carbon crucible, followed by the addition of 0.6 g of CsCl flux. The crucible was then loaded into a 14/16 mm I.D./O.D. fused silica ampule and flame-sealed under vacuum. The sealed ampule was placed in the muffle furnace, heated to 800 °C for 12 h, dwelled for 72 h, and then naturally cooled down to room temperature. After the reaction, the ampule was opened under ambient conditions, and the crucible was immersed in water for 2 h to fully dissolve the CsCl flux salt. The product was filtered, washed with water, and dried overnight in the air. $Ni_2P$ single-phase powder with a gray color was thus obtained.

### $Ni_3P$ Synthesis

To form a single phase of $Ni_3P$ a slight excess of Ni was necessary to prevent the formation of $Ni_{12}P_5$. Adding a few crystals of iodine was helpful to homogenize the products and convert the excess Ni to $NiI_2$, which is soluble in water. The 3.25:1 ratio of Ni:P, with a total weight of 300 mg and a few iodine crystals, was loaded into the 9/11 mm I.D./O.D. silica ampule and flame-sealed under vacuum. The reaction ampule was heated to 800 °C for 12 h and dwelled for 72 h. Then, the ampule was opened, and the products were washed in water to remove the $NiI_2$ formed during the reaction. After filtering and


https://doi.org/10.1021/jacs.6c01756
J. Am. Chem. Soc. 2026, 148, 10241−10256

drying, the single-phase $Ni_3P$ powder with a gray color was obtained.

### XAS Reference Samples

Elemental Ni powder (99.995%, Alfa Aesar), $K_3PO_4$ (Thermo Scientific, 96%), and $NaPH_2O_2{\cdot}H_2O$ (Thermo Scientific, 97+ %) were used as references for Ni and P *K*-edge XAS. NiO was synthesized in the lab by heating elemental Ni powder loaded in an alumina crucible at 1000 °C for 2 h in air.

### Preparation of High-Density Pellets for Ni *K*-Edge Studies

The as-synthesized $Ni_2P$ powder was pressed into a highly dense pellet by means of spark plasma sintering (SPS) using a Dr. Sinter Lab Jr. SPS-211Lx (Fuji Electronics Industry Co., Ltd.). For this purpose, 550 mg of $Ni_2P$ powder was introduced into a 10 mm graphite die, and tungsten carbide (WC) plungers were inserted at the top and bottom sides of the sample. Two graphite sheets were placed between the sample and the plunger to prevent direct contact and spilling of the sample. The assembly was placed into the SPS chamber and evacuated to below a pressure of 1 Pa. Then, a partial pressure of Ar gas was introduced into the chamber to prevent vaporization of volatile phosphorus during the sintering. A small pressure of 10 MPa was applied at room temperature to provide better heat transfer within the sample. The sample was heated to 600 °C in 8 min, and then the pressure was increased to 150 MPa. After 10 min of dwelling at 600 °C, the pressure was released, and the sample was naturally cooled down to room temperature. After taking the pellet out of the die, both sides were polished with 600, 1500, and 2500 grits of sandpaper to achieve a height of the resultant pellet of 1 mm for further *operando* electrochemical cell fabrication. The geometric density of the pellet was estimated to be 93.3%, while the Archimedes' density was measured to be 94.8%. The prepared $Ni_2P$ pellets were cut into 2.9 mm × 9.9 mm rectangular bars—shape required for the *operando* electrochemical cell preparation. For fine polishing, the cut $Ni_2P$ bars were molded with epoxy and dried overnight. The molded $Ni_2P$ bar was polished with a 600 grit SiC disk using a GP-25 grinder polisher (LECO) to remove the epoxy and expose the surface, and then the sample was polished sequentially using 1200 and 2500 grit SiC disks. After that, the sample was polished with 5 and 1 $\mu$m diamond suspensions and finally polished with a 50 nm alumina suspension. In between polishings, the sample was sonicated in water and ethanol for 2 min each. The resultant as-polished bar was retrieved from the mold by carefully cutting the epoxy resin with saw.

For $Ni_3P$, a similar SPS pressing procedure was performed using a 4 mm WC die and plungers. The as-synthesized $Ni_3P$ powder was loaded into the 4 mm WC die, and a pressure of 160 MPa was applied before thermal treatment. The pellet was heated to 575 °C for 8 min and dwelled for 10 min. Once the temperature reached 575 °C, the pressure was gradually increased to 600 MPa. After dwelling, the pressure was released, and the pellet was naturally cooled down to room temperature.

Our trials indicated that $Ni_3P$ pellets were not suitable for *operando* cell assembly due to their brittle nature. Thus, $Ni_3P$ pellets were used only for *ex situ* grazing incidence XAS. Two $Ni_3P$ pellets were prepared and polished with 600, 1500, and 2000 grit SiC sandpapers. To test HER, one of the pellets was attached to the Au wire with conductive H20E epoxy (Epoxy Technology) and cured in a vacuum oven at 150 °C for 20 min. The assembly was then molded in nonconductive epoxy. For the sample before HER, a pellet without Au wire was also molded in nonconductive epoxy under the same conditions. Both pellets embedded in epoxy were finely polished with the same procedure as $Ni_2P$ pellet. After polishing, the pellet with Au wire was tested for HER. Both pellets embedded in the epoxy were directly mounted at the beamline for the Ni *K*-edge GIXAS measurement.

### *Operando* Electrochemical Cell Preparation for Ni *K*-Edge

The custom-made cell assemblies were prepared by adapting the method developed by Drisdell's group (Figure S2).[45,46] The polished $Ni_2P$ bars were mounted on top of the cell as the working electrode to be exposed to the electrolyte and synchrotron X-ray. Two parallel 50 $\mu$m Pt wires were used as the counter electrode on top of the sample with >200 $\mu$m separation, and an Ag/AgCl reference electrode was inserted from the bottom side of the cell. The cell assembly was covered with polyimide film using 5 min of Double Bubble epoxy (Hardman) to prevent the electrolyte from leaking. The as-fabricated electrochemical cell was used for the Ni *K*-edge study.

### Electrochemical Measurements for Ni *K*-Edge

Using an SP-300 potentiostat (Bio-Logic), the *operando* electrochemical cell was operated in a three-electrode system with an Ag/AgCl reference electrode (LF-1-45, Innovative Instruments, Inc.) that was inserted at the bottom of the cell filled with electrolyte (0.5 M $H_2SO_4$). The flow system was attached to the cell, but eventually, it was not used due to the high noise that occurred during the XAS data collection. The cause of the noise may have been the electrolyte layer being thicker than 200 $\mu$m due to a lower than-ideal sample height induced by polishing. Because of time limitations at the beamline, we could not test other *operando* samples with different heights. Before the *operando* measurement, the cell was activated with 10 scans of cyclic voltammetry (CV) in a range of −0.01 to −0.41 $V_{RHE}$ [reversible hydrogen electrode (RHE)] with a scan rate of 5 mV/s. Chronoamperometry was conducted with an applied potential of −0.16 $V_{RHE}$ for 15 min to collect the *operando* XAS signal. The geometric surface area of the working electrode was ≈0.3 $cm^2$.

### *Operando* Grazing Incidence X-Ray Absorption Spectroscopy (GIXAS) for Ni *K*-Edge

To obtain surface-sensitive information, grazing incidence XAS studies at the Ni *K*-edge were performed at the 11-2 beamline at the Stanford Synchrotron Radiation Lightsource (SSRL). The X-ray beam was controlled by using a Si(220) double crystal monochromator and calibrated by adjusting the maximum point of the first derivative of the spectra at 8333 eV using a Ni foil reference. The fluorescence signal was collected using a Pilatus 100K detector system (Dectris) equipped with a 100-element Ge solid-state detector array, which was placed at 90° to the incident beam. To estimate the angle of the beam relative to the sample, the intensity of the incident beam was probed while the goniometer adjusted the angle of the cell. The EXAFS data were measured at two different angles of 0.08° and 10° at OCP, and XANES data were collected at 0.08° for *the operando* study. The data acquisition time for a single spectrum was ≈13 min for XANES and ≈32 min for EXAFS. For *ex situ* measurements and references, two scans were averaged, while for operando studies, one scan was collected. The collected data were merged and normalized using the Sixpack software package


https://doi.org/10.1021/jacs.6c01756
J. Am. Chem. Soc. 2026, 148, 10241−10256

and further processed using the Athena software package.[47] Raw scan data and processed files are provided in the Supporting Information.

### $Ni_3P$/Ni Foam Synthesis for P *K*-Edge Studies

The phosphorization of Ni foam (Heze Jiaotong, 110 pores per inch, 0.3 mm thick) was conducted to create a thin phosphide layer. The Ni foam was cut into a circular shape with a diameter of 20 mm to fit into an *operando* electrochemical cell. Ni foam and red P powder (100:$x$ molar ratio, $x$ = 1, 3, 5) were loaded into a 20 mm (I.D.)/23 mm (O.D.) silica ampule. P was added first, and then broken silica pieces were placed on top of the P to prevent direct contact between the Ni foam and P. Direct contact areas may result in an undesirably thick phosphide layer. On top of the silica pieces, the three Ni foam disks were placed, with the expectation that thinner phosphide layers would form on the foams located further away. Note that the weight of the Ni foam used for the molar ratio was the total weight of the three Ni foams. Further characterization showed that the second and third Ni foam disks barely reacted with P, and a noticeable P layer was formed only on the Ni foam disk closest to P. After placing the Ni foams, a 17/19 mm I.D./O.D. silica ampule was used as a plug by flipping it upside down and inserting it into the larger sample ampule. The whole assembly was evacuated and flame-sealed. To ensure a quick phosphorization reaction, the furnace was preheated to 800 °C, and the sealed ampule was placed in the furnace at 800 °C (*see safety warning at the beginning of the Experimental Section*) and annealed for 3 h. After that, the ampule was quenched in water. The ampule was opened in air, and Ni−P foam was obtained. The first layer of the reacted Ni foam, which was closest to the P, was used in this study.

### *Operando* Electrochemical Cell Preparation for P *K*-Edge

For the *operando* P *K*-edge experiment, a commercial R/T/A Spectro electrochemical cell (redox.me) was used. Ni−P foam was placed in the cell and covered with a 5 $\mu$m polypropylene film to prevent electrolyte leakage and avoid high attenuation of the incident X-ray beam. A tantalum foil was placed before the sample with contact to provide the connection to the working electrode plug. A rubber O-ring was placed between the film and the sample holder, and it effectively prevented the thin polypropylene film from leaking. A saturated calomel electrode (SCE) was used as the reference electrode, and a graphite rod was used as the counter electrode. To ensure continuous electrolyte flow, an NE-300 Syringe Pump (New Era Pump Systems Inc.) was connected to the inlet of the cell. It prevents the lowering of the electrolyte level as hydrogen bubbles accumulate within the cell.

### Electrochemical Measurements for P *K*-Edge

The *operando* cell was operated in a three-electrode configuration using an SCE as the reference electrode and a graphite rod as the counter electrode. The potentiostat used was the SP-300 (Bio-Logic), and the electrolyte was 0.5 M $H_2SO_4$. The Ni−P foam sample was activated with 10 cycles of CV in a range of −0.07 to −0.33 $V_{RHE}$ with a scan rate of 5 mV/s. Then, chronoamperometry was performed at an applied potential of −0.23 $V_{RHE}$ for 30 min to collect the *operando* signal.

### *Operando* XAS for P *K*-Edge

*Operando* XAS for the P *K*-edge experiment was performed at the 14-3a beamline at SSRL. The X-ray beam was controlled by using a Si(111) double crystal, and the beam was calibrated using the tetraphenylphosphonium bromide reference. The fluorescence signal was collected using a Vortex 4-element silicon drift detector (Hitachi High-Technologies Science), which was mounted at 90° to the incident beam. The sample and the beam source were sealed with a bag that was purged and filled with He to prevent attenuation of the X-rays by air. The measurement time was ≈13 min for XANES and ≈24 min for EXAFS per scan. The collected data were merged, normalized, and processed using the Athena software package.[47]

### Powder X-Ray Diffraction (PXRD)

The PXRD data was collected using a benchtop MiniFlex600 diffractometer (Rigaku) with Cu $K_\alpha$ radiation ($\lambda$ = 1.5418 Å) and a Ni $K_\beta$ filter. A zero-background Si holder (Rigaku) was used for sample loading. Further analysis of the collected data was performed using the Rigaku PDXL software package.

### X-Ray Photoelectron Spectroscopy (XPS)

XPS measurements were performed on an ESCALAB 250 Xi system (Thermo Scientific), equipped with a monochromated Al $K_\alpha$ X-ray source (1486.6 ± 0.2 eV), a hemispherical electron energy analyzer, an automated sample stage, and a video camera for viewing the analysis position. The standard analysis spot of about 650 × 650 $\mu m^2$ was defined by the microfocused X-ray source. The measurements were performed at room temperature in an ultrahigh vacuum chamber with a base pressure of $<5 \times 10^{-10}$ mbar. Pass energies of 150 and 40 eV were employed for the collection of survey and high-resolution spectra, respectively, with energy step sizes of 1 eV (survey) and 0.1 eV (high-resolution). Depth profiling was conducted using a MAGCIS $Ar^+$ ion gun (Thermo Scientific) in monatomic mode with a kinetic energy of 1 keV. All the collected spectra were processed with the CasaXPS software package.

### Atomic Force Microscopy (AFM)

The surface topography of the $Ni_2P$ pellet was characterized by a Cypher ES atomic force microscope (Oxford Instruments). A 160AC-NA cantilever (300 kHz, 26 N/m, OPUS by MikroMasch) was used for tapping mode imaging with a setpoint of 800 mV and a scan rate of 2 Hz. Post-analysis was conducted using the Gwyddion 2.67 software package.

### Scanning Electron Microscopy (SEM) and Energy-Dispersive X-Ray Spectroscopy (EDX)

To analyze the cross-sections of Ni−P foams, a Quanta 250 field emission SEM (FEI) was used with an X-Max 80 EDX detector (Oxford Instruments). The utilized voltage was 15 kV, and the collected data were processed using the Aztec software package. For sampling the cross-section of Ni−P foams, samples were molded in epoxy, polished with 800, 2000, and 4000 grits, and then finished with 0.5 $\mu$m diamond dispersions. The surface was coated with carbon to increase the conductivity of the sample. The presence of $Ni_3P$ was further revealed by SEM−EDX using a Quanta 3D field-emission FIB/SEM (FEI) equipped with an EDAX Octane Elect Plus detector.

### Transmission Electron Microscopy (TEM)

TEM specimens were prepared by using a Thermo Fisher Scientific (TFS) Helios G4 UC focused ion beam (FIB) instrument. $Ga^+$ ions at 30 kV and 16 kV were used for coarse polishing, while the final polishing was done at 5 kV, followed by Ar+ cleaning using a DuoMill 600 instrument (Gatan).


https://doi.org/10.1021/jacs.6c01756
J. Am. Chem. Soc. 2026, 148, 10241−10256

TEM, including electron diffraction (ED) and high-angle annular dark field scanning TEM (HAADF–STEM) studies, was performed using a TFS Themis Z 80–300 aberration-corrected (at the probe side) electron microscope operated at 300 kV. The microscope is equipped with SuperX$^{(TM)}$ EDX and Gatan Continuum 1065ER EELS detectors.

### DFT Calculations

DFT calculations were performed using the Vienna *ab initio* simulation Package (VASP).[48,49] Both spin-polarized and non-spin-polarized calculations were performed due to the presence of Ni; however, no spin polarization was observed in either $Ni_2P$ or $Ni_3P$. The exchange-correlation functional by Perdew, Burke, and Ernzerhof (PBE), with a kinetic energy cutoff of 520 eV, was used for the plane-wave basis set.[50] The choice of PBE over the local-density approximation (LDA) or meta-GGA follows the justification provided by Söderling, Giese, and coworkers.[51−53] Experimental structures were taken from ICSD.[54] Structural relaxation of atomic coordinates was performed until the total energy and forces converged to $10^{-6}$ eV and $10^{-3}$ eV/Å, respectively. Monkhorst–Pack *k*-mesh grids of 6 × 6 × 7 ($Ni_2P$) and 3 × 3 × 6 ($Ni_3P$) were used to sample the Brillouin zone during relaxation, with the meshes doubled for charge self-consistency and electronic-structure property calculations.[51,55] Gaussian smearing of 0.01 eV was used for total-energy calculations, whereas smearing of 0.15 eV was used to determine the density of states (DOS) evaluations. VASPKIT was used to analyze the DOS and charge density differences.[56]

VASP was also used to determine the structural properties of the $Ni_2P$ (0001) surface with and without adsorbed hydrogen for XANES simulations. Surface energies of the two terminations by cleavage ($Ni_3P_1$ and $Ni_3P_2$) were found using the method introduced by Tian et al., which reports surface energies that are invariant with the chemical potential of constituents.[57] The surface energy of the $Ni_3P_2$ termination is significantly higher (1.465 J/m$^2$) than the $Ni_3P_1$ termination (1.099 J/m$^2$). Using the $Ni_3P_1$ termination as the pristine model, we generated two models of adsorption. The first model simulated adsorption at very low coverage (0.84 atoms/nm$^2$) such that adsorbate–adsorbate interactions may be ignored, and hydrogen was found to stabilize in the 3-fold Ni *Hollow* sites. This required the generation of a large supercell to ensure a 10 Å separation between the adsorbate and its periodic image to avoid adsorbate–adsorbate interactions. The second model simulated adsorption at high coverage (20.19 atoms/nm$^2$) such that adsorbate–adsorbate interactions become dominant, and hydrogen was found to stabilize in the Ni–Ni *Bridge* sites. Selection of these specific adsorption sites is discussed elsewhere.[58,59] Structural relaxation of atomic coordinates was performed with slight differences to the bulk, such that the total energy and forces converged to $10^{-5}$ eV and $10^{-1}$ eV/Å, respectively. During surface-energy calculations, Monkhorst–Pack *k*-mesh grids of 7 × 7 × 1 were used to sample the Brillouin zone during relaxation, with the mesh of 15 × 15 × 2 used for charge self-consistency. For calculations involving large supercells, the *k*-mesh grid was reduced to (3 × 3 × 1) during relaxation and subsequently increased to (7 × 7 × 2) for charge self-consistency.

### XANES Simulations

The XANES simulations were performed with FEFF10.[60] The structural models for the simulations were generated from the VASP outcome described above for the pristine, low coverage, and high coverage cases.[58,59] The SCF stage used a cutoff radius of 5 Å, and the FMS stage used a cutoff of 9 Å, with default maximum angular momenta for all atoms at both the SCF and the FMS levels. These values ensured convergence for all of the model cases. All calculations used the final state rule approximation for the core hole and the many-pole approximation for the self-energy, using the atomic form of the optical constants.[60] To account for the sampling of both surface and subsurface atoms in the experiment, the difference spectra were computed by using the following weighted averages: $\Delta XAS = x \times (T_s - R_s) + (1 - x) \times (T_{ss} - R_{ss})$ where $T$ and $R$ are the target and reference spectra (e.g., the high coverage vs the pristine), respectively, for the surface ("*s*") and subsurface ("*ss*"), and $x$ is the fraction of surface spectra used in the weighted average.

A conservative spline was applied to the experimental data to reduce noise and improve the *L*2 normalization. Both absolute $\Delta\mu$ and relative $\Delta\mu/\mu$ spectra were analyzed. For normalization, the pre-edge and postedge ranges were carefully selected to ensure qualitative comparison of the spectra without introducing any artifacts in edge position or white line intensities. For all four spectra, a pre-edge range of −190 to −65 eV and normalization (postedge) ranges of +35 and +250 eV with respect to $e_0$ of 8333 eV were used (Figure S18). A normalization order of 3 was used for all spectra. Normalization factors were computed in the energy range of 8325–8357 eV as $Norm = 1/\text{mean}(\text{abs}(\Delta\mu))$, such that the normalized spectrum was $\Delta\mu^{NORM} = \Delta\mu \times Norm$. Analyses of relative $\Delta\mu/\mu$ spectra provided no improvement to the fits, and the absolute $\Delta\mu$ will be discussed in the manuscript.

## RESULTS AND DISCUSSION

### Crystal and Electronic Structures of $Ni_2P$ and $Ni_3P$

In this study, we pursued *operando* XAS studies for both Ni-*K* and P-*K* edges of the Ni–P hydrogen evolution catalysts. These edges have drastically different energies, namely, 8.3 and 2.1 keV. The *operando* measurements for such different energies require distinct sample preparation methods and unique sample environments. We focused on metal-rich nickel phosphides, $Ni_2P$ and $Ni_3P$ that have certain similarities. For Ni-*K* edge *operando* GIXAS studies, $Ni_2P$ pellets appeared more suitable, while $Ni_3P$ pellets were too brittle and demonstrated degradation under irradiation by a hard ≈8.3 keV X-ray beam. In turn, for the low-energy 2.1 keV P-*K* edge studies, bulk pellets and grazing incidence are not suitable, and we switched to the supported Ni foam samples where $Ni_3P$ was the produced phosphide. This complementary approach maximizes the surface sensitivity of bulk samples prepared as powder and supported foam. Although $Ni_2P$ and $Ni_3P$ are compositionally different, they both share common structural motifs. Therefore, we hypothesize that the observed trends may be transferable between the two catalysts. Multiple computational studies of the electronic structure and nature of the H adsorption sites for $Ni_2P$ and $Ni_3P$ show that, for both catalysts, $Ni_3$ hollow sites are the preferential adsorption sites for low H coverage. These studies also pointed to directions for potential improvement of the electrocatalytic performance, such as P enrichment of the surface and aliovalent substitutions.[33−35,61−66] $Ni_3P$ HER activity was demonstrated in numerous studies in the form of bulk material, standalone hollow nanoparticles, and $Ni_3P$/Ni composite nanoparticles.[33,67,68]



https://doi.org/10.1021/jacs.6c01756
J. Am. Chem. Soc. 2026, 148, 10241−10256

The crystal structures of two Ni−P catalysts studied here, $Ni_2P$ (structure type: $Fe_2P$, space group: $P\bar{6}2m$) and $Ni_3P$ (own structure type, space group: $I\bar{4}$) are composed of similar structural motifs, P@$Ni_9$ polyhedra, where each P atom is surrounded by nine Ni atoms (Figure 1a). The difference lies in the connectivity of the polyhedra: in $Ni_2P$ crystal structure, P@$Ni_9$ polyhedra share edges and faces, while in the structure of $Ni_3P$ corner and edge-shared P@$Ni_9$ polyhedra are present. Two P@$Ni_9$ polyhedra of $Ni_2P$ possess a longer average Ni−P bond length and larger volume than those of $Ni_3P$. The bulk electronic structure of the two catalysts is shown in Figure 1b, and the band structures can be found in Figure S1. Due to the increased P:Ni ratio in $Ni_2P$, the contribution of P states to the DOS near the Fermi level ($E_F$) is greater than that in $Ni_3P$. Although the DOS at $E_F$ for $Ni_2P$ is larger than that for $Ni_3P$, the 3*d*-band center position of $Ni_3P$ is higher than that of $Ni_2P$. These crystal and electronic structural similarities make the two materials active HER catalysts.

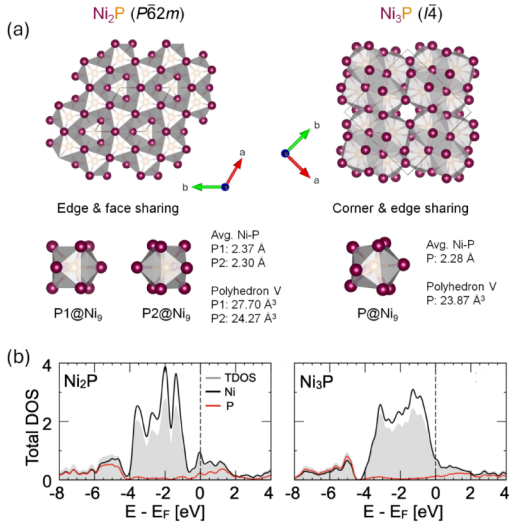


**Figure 1.** (a) Crystal structures and (b) total and projected density of states (DOS) of (left) $Ni_2P$ and (right) $Ni_3P$. Both structures are composed of P@$Ni_9$ units but differ in their connectivity: $Ni_2P$ features edge- and face-sharing, whereas $Ni_3P$ exhibits corner- and edge-sharing.

## *Ex Situ* Surface Studies of Ni−P Catalysts before and after HER

Figure 2 shows the surface states of $Ni_2P$ (pellet) and $Ni_3P$ (foam) catalysts before and after the HER, as probed by XPS measurements. Both samples are identical to those used for *operando* XAS studies. Before HER, the difference between $Ni_2P$ and $Ni_3P$ can be seen in the binding energy of the intermetallic Ni component, which is located at 853.6 eV ($Ni_2P$) and 852.6 eV ($Ni_3P$) (Figure 2a,c). Both values are higher than that of metallic Ni, representing the contribution of Ni−P bonding with partial charge transfer from more electropositive Ni to electronegative P. An increase in the P:Ni ratio should promote this charge transfer, thus explaining the higher Ni binding energy for $Ni_2P$ compared to $Ni_3P$. The position of the P 2p peak from intermetallic phosphide further confirms this electron transfer trend, as it appears at 130.0 and 129.4 eV for $Ni_2P$ and $Ni_3P$, respectively (Figure 2b,d). The higher number of Ni atoms in $Ni_3P$ results in greater electron transfer to P, lowering the binding energy compared to that of $Ni_2P$.

For the as-synthesized and air-exposed samples, the oxide contribution to the Ni 2p spectrum in $Ni_2P$ is lower than that in $Ni_3P$, indicating a higher resistance to oxidation by air, which agrees with a previous report on corrosion for various Ni−P catalysts (Figure 2a,c).[69] Nonetheless, after HER, both catalysts underwent significant surface oxidation, as the metallic components of Ni and P were drastically diminished and the oxidized species dominated the Ni 2p and P 2p spectra (Figure 2, top). These results demonstrate the formation of the surface oxide after HER and indicate that similar surface reconstruction processes occur in $Ni_2P$ and $Ni_3P$ during HER.

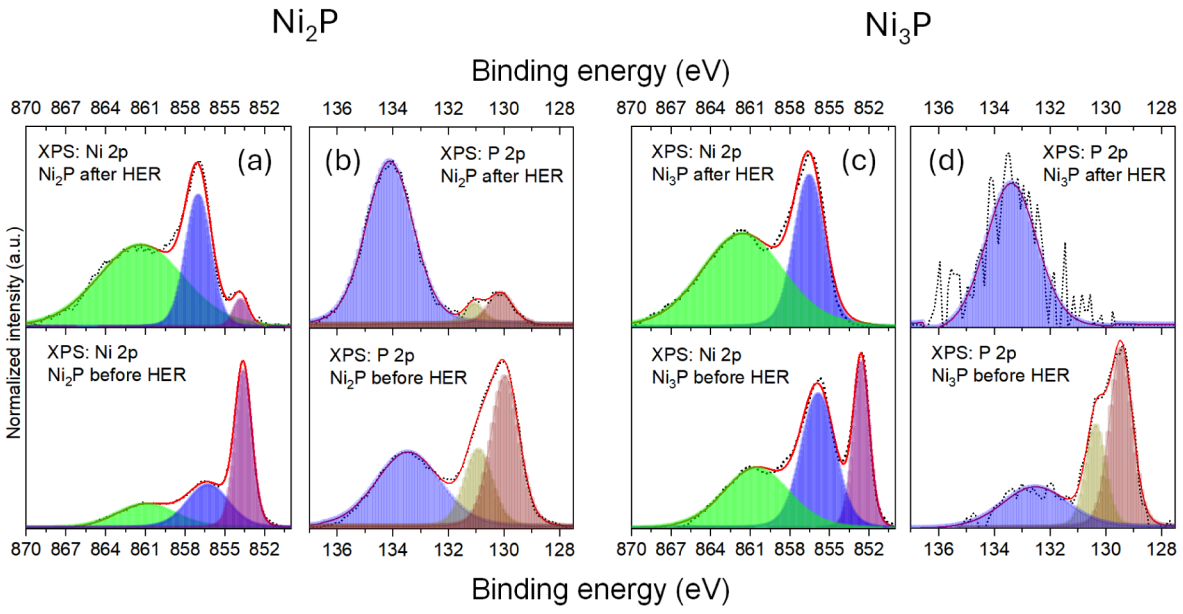


**Figure 2.** High-resolution Ni 2p (a, c) and P 2p (b, d) XPS spectra of $Ni_2P$ (a, b) and $Ni_3P$ (c, d). Bottom panels represent the surface states of the catalysts before HER (i.e., as-synthesized and air-exposed), while top panels represent the surface states after HER (i.e., HER tested, removed from acidic electrolyte, water-rinsed, and dried in air).



https://doi.org/10.1021/jacs.6c01756
J. Am. Chem. Soc. 2026, 148, 10241−10256

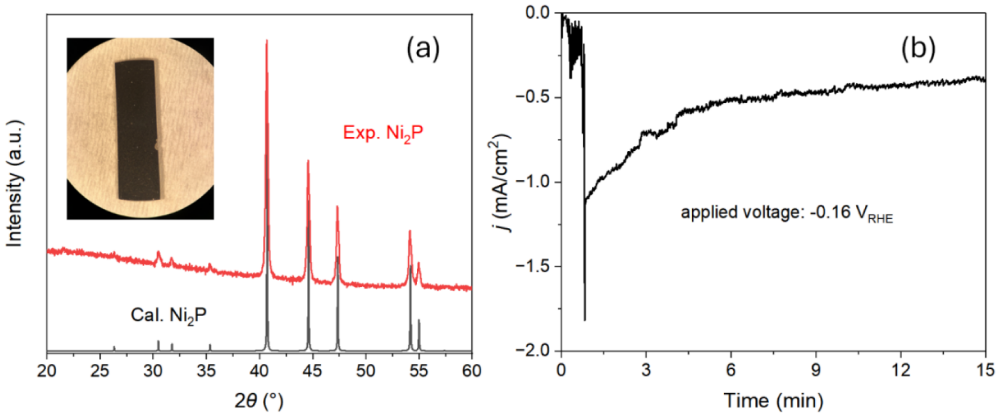


**Figure 3.** (a) The calculated (black) and experimental (red) PXRD patterns of the as-synthesized $Ni_2P$. The inset photo in (a) is the resultant $Ni_2P$ bar after fine polishing. (b) Chronoamperometry (CA) HER measurement of $Ni_2P$ catalyst bar mounted on the *operando* electrochemical cell.

Interestingly, the $Ni_2P$ surface still exhibits minor intermetallic components of Ni and P after HER, suggesting its higher resistance to oxidation. Because these XPS measurements were performed under *ex situ* conditions, they only reflect the surface state of the catalysts in the absence of electrolyte after HER. The mechanism of oxide formation and the true state of the active sites, therefore, need to be elucidated through *operando* measurements.

For *operando* XAS measurements, the catalyst powders need to be pressed into dense pellets and cut into the appropriate shape to be assembled in an *operando* electrochemical cell.[45] However, $Ni_3P$ pellets were found to be too brittle to be cut. Although further development of cell design may enable *operando* Ni *K*-edge studies of $Ni_3P$ in the future, such modifications are beyond the scope of this work. *Ex situ* GIXAS measurements on $Ni_3P$ show that the surface is altered by an X-ray beam. On the contrary, $Ni_2P$ exhibited a ductile nature, and no surface degradation during the *ex situ* GIXAS measurements was observed; thus, $Ni_2P$ was chosen for the preparation of cell assemblies and *operando* GIXAS measurements.

## $Ni_2P$ Synthesis and Sampling for*Operando* measurements

$Ni_2P$ was synthesized via the solid-state route with salt flux (CsCl) to facilitate the diffusion of the reactants. Since a $Ni_3P$ minor phase was formed with the exact stoichiometric Ni:P ratio of 2:1, 3% excess P was required to form the phase-pure $Ni_2P$. A carbon crucible was used as a reactor to prevent the reaction between the salt flux and silica, which might contaminate the products. After the reaction, the salt flux was removed by dissolving it in water, and a single phase of $Ni_2P$ powder was obtained. As shown in Figure 3a, the experimental PXRD pattern of the as-synthesized $Ni_2P$ matches the calculated pattern.

The common method of preparing an *operando* electrochemical cell for XAS is chemical vapor deposition of a single element. Deposition of metal phosphides in the same way is challenging because of the difficulties of working with toxic $PH_3$ as the P source. Although some films of complex phosphides, such as $CaZn_2P_2$, have been synthesized using phosphine,[70−72] commonly, a second post-treatment for phosphorization is conducted after depositing the metal element.[73,74] Such methods require the development of a sophisticated synthetic procedure for each specific phosphide. Hence, we targeted a process that would allow any bulk phosphide materials to be studied.

We have developed a top-down approach that produces pellets with smooth surfaces from bulk polycrystalline powder, allowing the surface to be examined through grazing incidence XAS. The single-phase $Ni_2P$ powder was sintered into a highly dense pellet using SPS and cut into a regular-shaped bar to fit into the *operando* electrochemical cell. No phase changes, such as decomposition, were observed during the flow test at a temperature (700 °C) higher than that used for sintering (600 °C) (Figure S3). Subsequently, the surface was polished down to a 50 nm alumina suspension. The inset of Figure 3a shows the resultant as-polished $Ni_2P$ bar. The surface roughness of the polished bar was estimated to be 12.2 nm, with a root-mean-square (RMS) of 2.7 nm, as determined by AFM studies (Figure S4). Notably, a smaller RMS roughness of the film, in the range of 1−2 nm, is preferred for GIXAS studies.[45] Although the surface of our polished pellet was rougher, the surface signal was still observable during the GIXAS measurements. Another previous study of thin CoP films measured bulk signals but still achieved surface sensitivity.[37] The polished $Ni_2P$ bar was mounted in the *operando* electrochemical cell as a working electrode and tested for the HER at the beamline (Figure S2). Figure 3b shows the chronoamperometry measurement conducted in a 0.5 M $H_2SO_4$ electrolyte aqueous solution. Current spikes were observed during the first minute, likely due to surface charging and species desorption. After reaching ≈1.8 mA/cm$^2$, the current density gradually decreased to ≈0.5 mA/cm$^2$ over 10 min and then stabilized, indicating consistent catalytic activity toward HER.

## *Operando* GIXAS Measurements of Ni *K*-Edge of $Ni_2P$ Catalysts

Regular fluorescent XAS measurement of the $Ni_2P$ bar would provide the signal mainly from the bulk as well as from the surface, with the latter being a minor component. To maximize the desired signal from the surface, GIXAS measurements were performed. One needs to ensure that the sample is suitable for GIXAS measurements and that surface-relevant information can be extracted. Figure S5 shows the *ex situ* Fourier-transformed Ni *K*-edge EXAFS spectra of bulk Ni, $Ni_2P$, and NiO reference materials, and the prepared $Ni_2P$ catalyst as a function of grazing angles. It was established that $Ni_2P$ bar prepared for *operando* electrochemical study is suitable for XAS measurement despite the high thickness of the sample (≈1 mm), which could generate self-absorption. At a grazing angle of 10°, the Ni−Ni and Ni−P radial distances of $Ni_2P$ catalyst under OCP (open circuit potential) were consistent with those


https://doi.org/10.1021/jacs.6c01756
J. Am. Chem. Soc. 2026, 148, 10241−10256

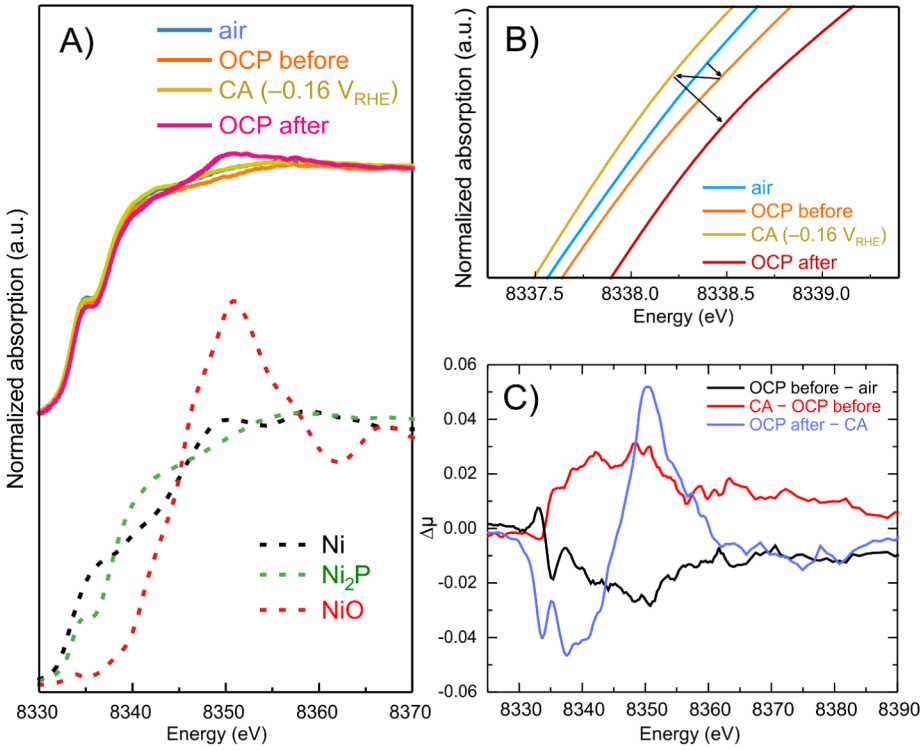


**Figure 4.** *Operando* XANES spectra of the Ni *K*-edge of $Ni_2P$ measured at 0.08° grazing incidence. (A) XANES spectra of the synthesized $Ni_2P$ under different conditions and reference materials (dashed lines vertically offset for clarity). "OCP before" represents the open circuit potential condition before HER testing, and "OCP after" represents the condition after turning off the applied potential. (B) The magnified edge area. (C) Difference spectra between subsequent spectra: air, OCP before, *operando* (CA), and OCP after conditions.

for the $Ni_2P$ reference, indicating that the collected XAS signal was mostly from the bulk. At a grazing angle of 0.08°, it was observed that the distance shortened as Ni−Ni and Ni−P bonding shifted toward a lower radial distance. The distance shortening may indicate some structural surface relaxation. Calculations of the relaxed surface layer of $Ni_2P$ in vacuum and with adsorbed species indicated substantial modifications of Ni−Ni and Ni−P distances. These results indicate that a grazing incidence angle of 0.08° is good enough to detect the surface signal for the *operando* electrochemical setup used in this study, and accordingly, all further XAS measurements were performed under this condition.

To investigate the behavior of $Ni_2P$ during HER in an acidic electrolyte, Ni *K*-edge XANES studies were performed (Figure 4). The XANES spectrum of the $Ni_2P$ catalyst measured under an air atmosphere is similar to the one for the $Ni_2P$ reference, but the intensity of the pre-edge region was more pronounced (Figure 4A). This could be due to the distortion effect from self-absorption as the sample concentration was higher compared to thin films (<100 nm) or diluted pellets.[75] However, since the acquired XANES data were measured under identical environments, the spectral differences observed under different electrochemical conditions should reflect the actual changes on the catalyst's surface. The broad features of the white line of $Ni_2P$ indicate the soft, polarizable nature of the P ligand. In Ni oxides or nitrides, highly electronegative and ionic N or O ligands sharpen the white line due to strong ligand effects.[32,76] When the $Ni_2P$ catalyst was immersed in the electrolyte under the OCP condition, the edge of the spectra moved to higher energy (Figure 4B,C). One can see that the experimental difference spectrum (OCP before − air) is not comparable to the reference difference spectrum ($Ni_2P$−NiO) (Figure S6A). Thus, the observed change cannot be attributed to the simple dissolution of surface NiO.

Application of a negative potential of −0.16 $V_{RHE}$ had the opposite effect, shifting the spectral edge toward lower energy, even lower than that of the as-prepared sample exposed to air (Figure 4B,C). A similar reduction of Ni sites was also observed on the Ni-doped $MoS_2$, electrodeposited Ni layer on the Pt surface, and $Ni_3S_2$ surfaces.[39,77,78] These results demonstrate that Ni sites in the $Ni_2P$ structure undergo reduction during HER in acidic conditions, with no evidence of oxide formation. This discloses the actual state of the Ni sites during the HER as intermetallic $Ni^0$, rather than an oxide or other oxygenated phases. To reveal when oxide forms, it is crucial to note that surface oxidation appeared immediately upon switching off the reducing bias (Figure 4). In the white line, an additional peak corresponding to NiO was formed at 8351 eV, and the edge position was shifted toward higher energy (Figures 4A,C and S6B). The difference curve of (OCP after − CA) is similar to the experimental reference difference curve (NiO−$Ni_2P$) (Figure S6B), thus confirming oxidation of surface Ni sites to NiO. Capturing the oxide signal of catalysts represents the surface sensitivity of the sample preparation method developed in this study. Formation of surface oxide was observed without applying the anodic potential. This finding explains why the surfaces of Ni−P catalysts are found to be severely oxidized after experiencing a cathodic potential during HER (Figure 2). A previous cathodic corrosion report also supports this observation.[79] Although intermetallic $Ni^0$ is an active site, the surface reconstruction developed under HER conditions promotes oxidation once the bias is removed. Wexler and coworkers calculated the surface phase diagram of $Ni_2P$ under an applied potential. When the potential is −0.2


https://doi.org/10.1021/jacs.6c01756
J. Am. Chem. Soc. 2026, 148, 10241−10256

$V_{RHE}$ or more than that, the P adatom would be adsorbed on $Ni_3$ hollow sites and form phosphine ($PH_3$).[35] We hypothesize that in the absence of the applied reductive potential, the active Ni−P−H surface component is promptly oxidized by an acidic electrolyte.

### *Ex Situ* GIXAS Measurements of Ni-*K* edge of $Ni_3P$ Catalysts

For comparison, *ex situ* Ni *K*-edge GIXAS measurements were performed on polished $Ni_3P$ pellets under conditions before and after the HER (Figure S8). The PXRD patterns of the as-synthesized $Ni_3P$ powder matched those of the calculated patterns (Figure S7a). For the "after HER" condition, the $Ni_3P$ pellet was subjected to chronoamperometry at an applied potential of − 0.16 $V_{RHE}$ for 1 h (Figure S7b). To probe the surface sensitivity, XANES spectra were inspected at two different grazing angles: 2.0° for the bulk and 0.1° or 0.08° for the surface (Figure S8a). For the bulk measurements (2.0°), the Ni *K*-edge XANES spectra of $Ni_3P$ catalysts before and after HER were found to be nearly identical. The corresponding difference spectrum revealed no notable changes (Figure S8b). At a lower grazing angle of 0.10°−0.08°, which probes the surface region, the XANES spectra of $Ni_3P$ before and after HER exhibited clear differences. First, both samples showed partial oxidation, represented by the enhanced white line intensity at 8350.8 eV corresponding to NiO. Second, the absorption edge of $Ni_3P$ after HER shifted further to higher energy compared to that before HER, indicating that the surface experienced oxidation after HER. The difference spectrum shows the drastic changes between the two surfaces (Figure S8b). These observations are in line with earlier XPS results of dominant surface oxidation on spent $Ni_3P$ catalysts. While these complementary *ex situ* XANES spectra of $Ni_3P$ confirm that surface oxidation of Ni−P catalysts after HER is universal, the *operando* XANES spectra of $Ni_2P$ explain when the oxide formation occurs (Figure 4).

### Simulation of XANES Spectra of Ni *K*-Edge for $Ni_2P$

We have recently performed a comprehensive experimental and theoretical investigation of the $Ni_2P$ surface terminations and established their structure and experimental trends in HER performance.[58,59] These data were used to create pristine, relaxed, and H-saturated $Ni_2P$ surfaces used for XAS simulations (Figure S19). To shed some light on the surface structure of $Ni_2P$ catalyst during HER, XANES spectra of the relaxed termination of the (0001) facet with pristine and full H coverage were simulated (Figure S9). The simulated difference spectra show that when the (0001) $Ni_2P$ surface is fully covered by H, it exhibits intensity in the positive region, which is in line with the difference spectra observed under CA conditions of experimental XANES. This indicates that adsorbed H atoms on the $Ni_2P$ surface cause the peak to shift to negative energy. Because of the penetration depth of incident X-rays, even with the GIXAS setup, the spectra were weighted with different ratios of surface and subsurface regions. It is noteworthy that while the $Ni_2P$ pellet used in *operando* XAS measurement is polycrystalline, exposing numerous different facets, the simulated spectra are built using only one (0001) facet, leading to a nonidentical peak shape. One clear trend from experimental XANES is the negative intensity of the difference spectra of "OCP before − air" and the positive intensity of "CA − air" or "CA − OCP before", as shown in Figures 4c and 5.

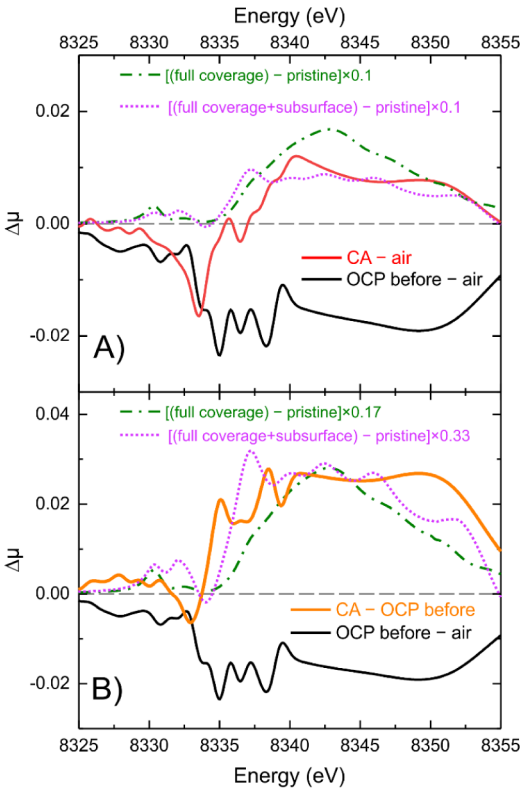


**Figure 5.** Comparison of the difference spectra of simulated and experimental XANES. Experimental data are shown as solid lines. The green dashed line corresponds to the simulated spectrum with full H coverage, while the pink dotted line corresponds to the full coverage simulated spectrum with a weight of 50% of surface and 50% subsurface regions. In (A), the difference operando curve in red is [CA − air], while in (B), the difference operando line in orange is [CA − OCP before]. Simulated difference spectra were scaled by the legend scaling factor.

Comparing the difference curves "CA − air" or "CA − OCP before" to simulations for a single H atom shows a poor match, indicating that the single H model is not representative of the actual state of the catalysts. In turn, the full coverage model agrees with the experimental spectra. When "CA − air" experimental curve is considered, similar L2 normalization fits for 100% surface and 50% surface + 50% subsurface spectra were obtained (Figure 5A). When the experimental difference curve "CA − OCP before" is considered, the model with a subsurface component provides a significantly better fit, well-representing major features (Figure 5B). Thus, the observed difference in XANES spectra is caused by the absorption of a substantial number of bridged H atoms to the surface on $Ni_2P$.

The results of simulated difference spectra for single H coverage show that the intensity is significantly lower than that of the fully covered surface (Figure S9). This suggests that the intensity of difference spectra is proportional to the concentration of adsorbed H on the surface. Under operando experimental conditions, a small overpotential was applied, which may lead to partial and not full H coverage. Yet, the number of adsorbed H was enough to cause the observed changes. It is still not clear what leads to the peak shift to higher energy during OCP beforehand, but from our simulations, it is not due to proton adsorption. We hypothesize that dissolved oxygen or sulfuric acid may interact with the surface Ni.[80,81]


https://doi.org/10.1021/jacs.6c01756
J. Am. Chem. Soc. 2026, 148, 10241−10256

### $Ni_3P$/Ni Foam Synthesis

Since the X-ray beam energy of the P *K*-edge (2.1 keV) is much lower than that of the Ni *K*-edge (8.3 keV), the same GIXAS measurement is not feasible to probe the P state *operando*. To collect the surface signal of P from the direct incident beam, a synthesis method was devised to make thin layers of nickel phosphide by reacting gaseous P with Ni foam for short periods of time. It was expected that the high surface area of Ni foam could enhance the signals from the surface. The phosphorization of Ni foam was done in vacuum-sealed silica ampules through a prompt solid−gas reaction. To prevent the phosphorus from reacting with the inner part of the Ni foam, the furnace was preheated to 800 °C (*see warning in the Experimental Section*) and the reaction ampule was placed in the preheated furnace for 3 h, followed by quenching in water. To optimize the thickness of the phosphide layer, three different molar ratios of Ni foam to P were used, namely, 100:1, 100:3, and 100:5 (Figure 6a). The inset of Figure 6a shows the Ni−P foam after the reaction. It was noted that all of the reacted Ni−P foam samples formed surface $Ni_3P$ and metallic Ni underneath, but the $Ni_3P$ content increased with the increase in the nominal P content. Further increasing the Ni:P molar ratio to 100:17 (≈6:1) formed a predominantly $Ni_3P$ phase (Figure S10). However, the 100:1 (Ni:P) molar ratio sample showed a negligible PXRD pattern of $Ni_3P$. TEM was performed on the reacted part of the Ni−P (100:1) foam after lamella sampling via FIB. The high-angle annular dark-field (HAADF)−STEM image clearly shows that the phase formed on Ni−P (100:1) foam has a 4-fold improper rotation axis, which corresponds to $I\bar{4}$ space group of $Ni_3P$ (Figure 6b).

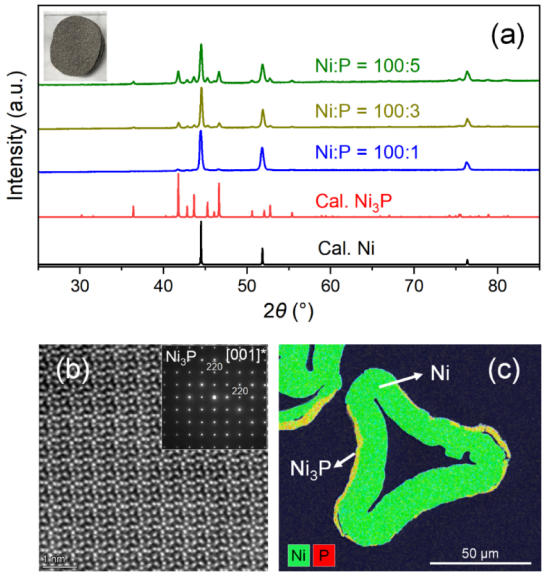


**Figure 6.** Structure and elemental analyses of the synthesized $Ni_3P$/Ni foams. (a) Experimental PXRD patterns of Ni−P foams reacted with different Ni:P molar ratios, which are 100:1 (blue), 100:3 (olive), and 100:5 (green), and calculated PXRD patterns of Ni (black) and $Ni_3P$ (red) phases. The inset shows an optical image of the as-synthesized $Ni_3P$/Ni foam (100:1). (b) [001]* HAADF−STEM image of $Ni_3P$/Ni foam produced from a 100:1 (Ni:P) molar ratio, and the inset figure is the corresponding SAED pattern. (c) SEM−EDX mapping of the cross section of the ligaments of the same foam. The green color represents Ni, the red color represents P, and the yellow color represents the mixed Ni and P.

The selected area electron diffraction (SAED) pattern shown in the inset of Figure 6b corresponds to the diffraction of $Ni_3P$ along the [001] zone axis. To measure the thickness of the phosphide layer, EDX analysis was performed for the cross-section of the foams (Figures 6c, S11 and S12). The phosphide layer was formed only on the surface of the foam ligaments, indicating that a quick solid-state reaction is suitable for the synthesis of a thin nickel phosphide layer covering the surface of the 3D tangled network of the Ni foam. The thickness of the nickel phosphide layer increased as the P ratio increased, and the average thickness was estimated to be approximately 2, 3, and 6 $\mu$m for the samples with 100:1, 100:3, and 100:5 Ni:P weight ratios, respectively. The thickness of the nickel phosphide layer of Ni−P foam (100:1) was further confirmed to be ≈2 $\mu$m by TEM cross-sectional imaging, as shown in Figure S13. The STEM−EDX spectrum also displays the proportional intensity of the Ni and P contents (Figure S14). Thus, we have prepared a thin layer of $Ni_3P$ phosphide supported on Ni foam. To maximize the surface contribution for the XAS signal, $Ni_3P$/Ni foam produced from the Ni:P (100:1) reaction was used for the *operando* electrochemical P *K*-edge XAS measurements. The detailed computational analysis of $Ni_3P$ pointed out the P adatom as the active site in HER, in analogy to the identified active site on $Ni_2P$.[33] Hence, we believe that $Ni_3P$ represents a good model system to investigate the evolution of surface P sites during the HER.

### *Operando* Electrochemical P *K*-Edge XAS Measurements of $Ni_3P$/Ni Foam

To test the HER activity of $Ni_3P$/Ni foam, the sample was mounted on the *operando* electrochemical cell (Figure S15). A syringe pump was connected to the cell inlet to ensure continuous refilling of the electrolyte. This was necessary to prevent hydrogen bubbles from pushing out the electrolyte and lowering the overall electrolyte level. Figure S16 shows the chronoamperometry measurements of pristine Ni and synthesized $Ni_3P$/Ni foams for 3 h. At an applied potential of −0.23 $V_{RHE}$, the HER activity of the $Ni_3P$/Ni foam was superior. The current density of Ni foam was 4.5 mA/cm$^2$ while that of $Ni_3P$/Ni foam was 6.4 mA/cm$^2$, which is about a 40% improvement. This demonstrates that the phosphide layer formed through a quick solid−gas reaction enhanced the HER activity of pristine Ni foam. Notably, the reported HER activity of $Ni_3P$ outperformed $Ni_2P$ and is comparable to $Ni_5P_4$ because of the stable P-enriched $Ni_4P_4$ surface termination.[33]

Figure 7a shows the cathodic polarization curve of $Ni_3P$/Ni foam measured at the beamline. The overpotential value required to drive the current density of −10 mA/cm$^2$ was estimated to be $\eta_{10}$ = 0.28 $V_{RHE}$. Figure 7b shows the chronoamperometry measurement of $Ni_3P$/Ni foam during the P *K*-edge XAS measurement. The small bumps at 7 and 15 min are because of the hydrogen bubbles pushing out some of the electrolyte, while the refilling was not 100% efficient. This may be attributed to the syringe pump being positioned lower than the cell due to space limitations at the beamline.

To elucidate the behavior of the P site of $Ni_3P$/Ni foam during acidic HER, XANES was measured under four different conditions: (*i*) as-synthesized, exposed to air; (*ii*) immersed in electrolyte (OCP before); (*iii*) *operando*, under applied potential (−0.23 $V_{RHE}$); and (*iv*) after turning off the bias (OCP after) (Figure 8). $K_3PO_4$ was used as a reference for the $P^{5+}$ oxidation state, and $NaH_2PO_2$ was used for the $P^{1+}$ oxidation state with P−H bonding.[37] Bulk powders of $Ni_3P$


https://doi.org/10.1021/jacs.6c01756
J. Am. Chem. Soc. 2026, 148, 10241−10256

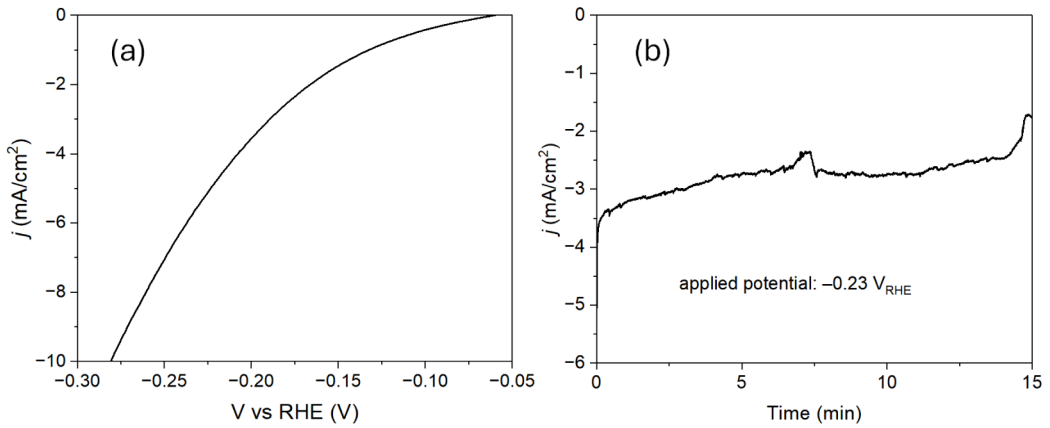


**Figure 7.** (a) Cathodic polarization curve and (b) chronoamperometry measurement of $Ni_3P$/Ni foam in the *operando* electrochemical cell (Figure S12) with an electrolyte flow rate of 10 mL/h.

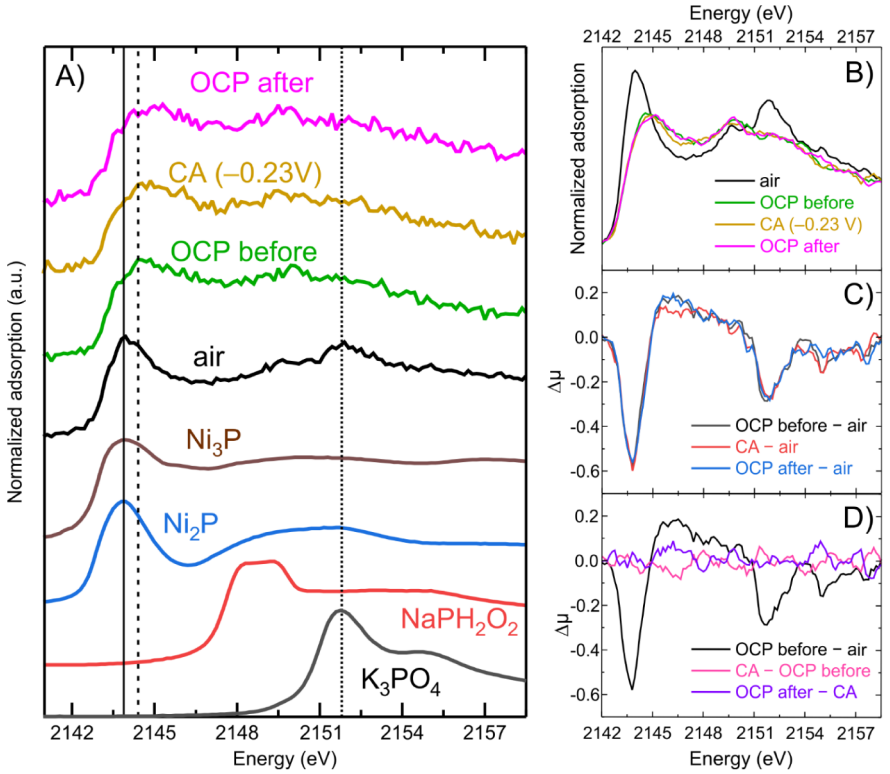


**Figure 8.** XANES spectra of the P *K*-edge of $Ni_3P$/Ni foam during acidic HER. (A) The bottom four curves are reference materials, and the top 4 curves represent the studied sample under indicated conditions. Black spectrum: as-synthesized exposed to air; green spectrum: sample immersed into electrolyte (OCP before); orange spectrum: *operando*, during HER (CA: chronoamperometry) under applied potential −0.23 $V_{RHE}$; and magenta spectrum: sample right after cathodic potential is turned off (OCP after). (B) The overlay of smoothed XANES spectra. (C, D) Difference XANES spectra produced by subtracting the spectra of the air condition (C) or previous condition (D).

and $Ni_2P$ were used as Ni phosphide references. Reference spectra show that the white line of $Ni_3P$ was broader compared to $Ni_2P$ emphasizing the impact of electronic structure (different for $Ni_3P/Ni_2P$) rather than local P coordination (similar for $Ni_3P/Ni_2P$) on the XAS spectra.[82] Air-exposed, as-synthesized $Ni_3P$/Ni foam shows a white line position similar to that of the $Ni_3P$ reference at 2143.9 eV (Figure 8a). $Ni_3P$/Ni foam exposed to air shows a hump of the $P^{5+}$ oxidized species of phosphate around 2151.9 eV, which is coincident with that of $K_3PO_4$, implying that the detected signal is from the sample surface. This observation is in line with a previous report from the Lewis group that CoP film had several oxidized phases on the surface, including $P^{5+}$.[37] The difference is that we did not observe oxidation states other than $P^{5+}$ in $Ni_3P$/Ni foam exposed to air. This could be due to the higher corrosion resistance of $Ni_3P$.[33]

Once $Ni_3P$/Ni foam was immersed in acidic electrolyte (OCP condition), the XANES spectra show significant changes as the main edge position shifted to higher energy, and the overall white-line intensity decreased and became broader (Figure 8). This indicates that the electronic state of P has changed due to ligand effects.[83] A previous report from Solomon's group described similar spectral changes of the S *K*-edge XANES induced by S−H bonding.[84] Such H bonding to


https://doi.org/10.1021/jacs.6c01756
J. Am. Chem. Soc. 2026, 148, 10241−10256

S weakens the covalency of the bonding between the central Fe atom and S, resulting in an overall reduction of white-line intensity and a shift of the peak toward higher energy. In analogy, adsorption of protons from the electrolyte on the P sites should reduce Ni−P covalency, leading to the spectral alterations observed here at the P *K*-edge. Several calculation reports show that P acts as a proton-acceptor due to its negative charge.[32,33,35] Our results confirm that the active P species in acidic 0.5 M $H_2SO_4$ aqueous electrolyte are different from the species under *ex situ* dry conditions. We have demonstrated that for another active phosphide HER catalyst, FeP, the initial adsorption of H occurs on P and not on Fe sites.[85] An additional effect of the acidic electrolyte is eliminating $P^{5+}$ component under OCP conditions, indicating that phosphate was decomposed or underwent reduction under the acidic electrolyte.[86,87]

P *K*-edge spectra retained a similar shape during the OCP before and after, and under *operando* conditions, once their initial alteration occurred. Difference spectra in Figure 8C,D show the considerable changes between the air and electrolyte (OCP before) environments, and then maintained similar features during HER (CA: chronoamperometry) and after turning off the bias (OCP after). The previous studies of P *K*-edge for CoP film also show no significant differences between OCP and *operando* conditions.[37] No drastic changes between the OCP and CA conditions could indicate the persistent role of P as a proton acceptor under the acidic media environment or insufficient resolution of the experiment to detect tiny changes. A hint of changes is visible in the difference spectrum between the air and CA conditions in the region of 2145.3−2147.2 eV (Figure 8C,D). However, the low signal-to-noise ratio precludes us from analyzing this feature. Further efforts will be dedicated to obtaining higher-quality operando P *K*-edge spectra of $Ni_3P$ and $Ni_2P$ and their detailed computational and simulation analysis.

Assuming that $Ni_2P$ and $Ni_3P$ studies are translatable to each other, Ni and P surface sites in Ni-rich phosphides exhibit different behavior (Figure 9). Ni sites are slightly affected by the electrolyte and then undergo a substantial change under *operando* conditions, while P seems to adsorb protons already upon immersion in acidic electrolyte and shows subtle changes between OCP and *operando* conditions. It was reported that the hydronium ion is adsorbed first to electronegative P sites but quickly migrates to Ni sites as it becomes a hydride ion once reduced.[32] However, the low signal-to-noise ratio of P *K*-edge spectra prevents the detection of differences in P surface sites during HER. The collected data indicate that the Ni active site during HER is intermetallic $Ni^0$ and oxidation occurs immediately once the applied potential is turned off. Complementary *ex situ* Ni *K*-edge GIXAS for the spent $Ni_3P$ catalyst exhibited a similar oxidation occurrence on the catalyst's surface after HER. Together, these results demonstrate how surface oxidation occurs in Ni−P catalysts during the HER process, consistent with the XPS results obtained for the spent catalysts.

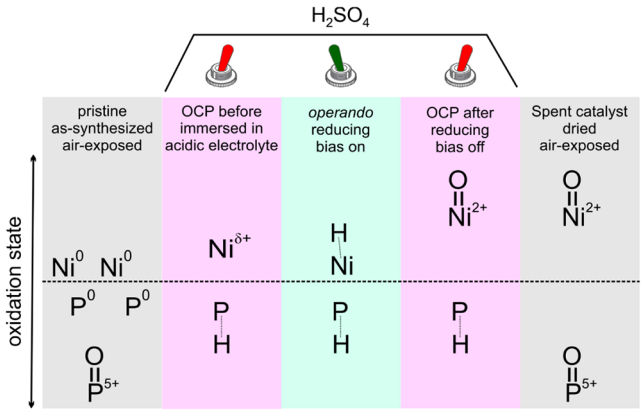


**Figure 9.** Summary for Ni−P catalysts' behavior from *ex situ* and *operando* XAS and *ex situ* XPS. $Ni^0$ and $P^0$ indicate the Ni and P states in the intermetallic Ni phosphide, not the elemental states.

Our observations allow us to explain the body of XPS surface analyses of pristine and used Ni−P HER catalysts.[30] In agreement with XPS observations, XAS experiments detected intermetallic Ni and P signals, as well as the presence of oxidized components in the as-prepared and air-exposed samples. We have observed that during HER, active reduced Ni species are formed, while P states remain intact after the adsorption of protons from the electrolyte takes place (Figure 9). Such Ni species align with models featuring a high coverage bridged H surface of (0001) termination. After the reductive bias is turned off, active surface sites are oxidized by sulfuric acid in the electrolyte and by air. For Ni, this leads to the prompt formation of Ni−O on the surface in the electrolyte. For P, the P−H phosphine-like species can be leached out from the surface upon oxidation.[35] This explains the substantial enrichment of the surface signal with Ni and depletion with P for the HER catalysts observed by us (Figure S17) and multiple other XPS studies.

## CONCLUSIONS

In this study, we have introduced two different sample preparation routes for *operando* XAS of Ni and P catalytically active sites from the $Ni_2P$ pellet and $Ni_3P$/Ni foam. It was demonstrated that both preparation methods were suitable to provide surface-relevant signals since clear changes in XANES spectra under different conditions were observed. Although after HER, the *ex situ* surface state of Ni in $Ni_2P$ structure is severely oxidized, we demonstrated that the active surface state during HER is intermetallic $Ni^0$, and oxidation occurs only after the HER applied potential is turned off. For P, immersion into the electrolyte formed a new P ligand environment, emphasized in the broadening and shifting of the P *K*-edge white line. This modified state remained consistent under *operando* conditions, indicating the role of P sites as proton acceptors throughout the reaction. The XANES spectra of these phases did not undergo noticeable changes during HER. Thus, the P active site during HER is different from the *ex situ* oxide state. We anticipate that these results may expand the scope of materials that can be used for *operando* XAS analysis (e.g., ternary intermetallic phosphides) and provide insight into sample preparation routes for practical applications.

## ASSOCIATED CONTENT

### Supporting Information

The Supporting Information is available free of charge at https://pubs.acs.org/doi/10.1021/jacs.6c01756.

Additional figures pertaining to band structures, atomic force microscopy, Fourier-transformed EXAFS data, powder X-ray diffraction, cross-section STEM images of TEM lamella, *operando* cell pictures, and chronoamperometry measurements (PDF)



https://doi.org/10.1021/jacs.6c01756
J. Am. Chem. Soc. 2026, 148, 10241−10256

An archive with raw XAS scan data and processed.prj XAS files (ZIP)

## AUTHOR INFORMATION


### Corresponding Author

**Kirill Kovnir** − *Department of Chemistry, Iowa State University, Ames, Iowa 50011, United States; Ames National Laboratory, U.S. Department of Energy, Ames, Iowa 50011, United States;* orcid.org/0000-0003-1152-1912; Email: kovnir@iastate.edu

### Authors

**Seongyoung Kong** − *Department of Chemistry, Iowa State University, Ames, Iowa 50011, United States; Ames National Laboratory, U.S. Department of Energy, Ames, Iowa 50011, United States*

**Ernesto Soto** − *Department of Chemistry, Iowa State University, Ames, Iowa 50011, United States; Ames National Laboratory, U.S. Department of Energy, Ames, Iowa 50011, United States;* orcid.org/0000-0001-5346-7382

**Jiyun Hong** − *Stanford Synchrotron Radiation Lightsource, SLAC National Accelerator Laboratory, Menlo Park, California 94025, United States;* orcid.org/0000-0002-3631-0559

**Ryan Davis** − *Stanford Synchrotron Radiation Lightsource, SLAC National Accelerator Laboratory, Menlo Park, California 94025, United States*

**Erik Nelson** − *Stanford Synchrotron Radiation Lightsource, SLAC National Accelerator Laboratory, Menlo Park, California 94025, United States*

**Vladimir Roddatis** − *GFZ Helmholtz Centre for Geosciences, Potsdam D-14473, Germany;* orcid.org/0000-0002-9584-0808

**Oleg I. Lebedev** − *Laboratoire CRISMAT ENSICAEN, CNRS UMR 6508, Caen F-14050, France*

**Weiran Zheng** − *Department of Chemistry and Guangdong Provincial Key Laboratory of Materials and Technologies for Energy Conversion, Guangdong Technion-Israel Institute of Technology, Shantou 515063, P.R. China; Technion-Israel Institute of Technology, Haifa 32000, Israel;* orcid.org/0000-0002-9915-6982

**Humphrey W. Odhiambo** − *Ames National Laboratory, U.S. Department of Energy, Ames, Iowa 50011, United States; Department of Materials Science & Engineering, Iowa State University, Ames, Iowa 50011, United States*

**Nakyung Oh** − *Ames National Laboratory, U.S. Department of Energy, Ames, Iowa 50011, United States; Department of Materials Science & Engineering, Iowa State University, Ames, Iowa 50011, United States*

**Vivek Upadhyay** − *Department of Chemistry, Iowa State University, Ames, Iowa 50011, United States*

**Natalia C. M. Spera** − *International Iberian Nanotechnology Laboratory (INL), Braga 4715-330, Portugal*

**Dhruv Raturi** − *Ames National Laboratory, U.S. Department of Energy, Ames, Iowa 50011, United States; Department of Materials Science & Engineering, Iowa State University, Ames, Iowa 50011, United States*

**Prashant Singh** − *Ames National Laboratory, U.S. Department of Energy, Ames, Iowa 50011, United States*

**Gaoyuan Ouyang** − *Ames National Laboratory, U.S. Department of Energy, Ames, Iowa 50011, United States*

**Fernando D. Vila** − *Department of Physics, University of Washington, Seattle, Washington 98195, United States;* orcid.org/0000-0002-6508-4896

**Simon R. Bare** − *Stanford Synchrotron Radiation Lightsource, SLAC National Accelerator Laboratory, Menlo Park, California 94025, United States;* orcid.org/0000-0002-4932-0342

**Yury V. Kolen'ko** − *International Iberian Nanotechnology Laboratory (INL), Braga 4715-330, Portugal;* orcid.org/0000-0001-7493-1762

**Duane D. Johnson** − *Ames National Laboratory, U.S. Department of Energy, Ames, Iowa 50011, United States; Department of Materials Science & Engineering, Iowa State University, Ames, Iowa 50011, United States*

Complete contact information is available at: https://pubs.acs.org/10.1021/jacs.6c01756


### Author Contributions

The manuscript was written through the contributions of all authors. All authors have given their approval to the final version of the manuscript.

### Notes

The authors declare no competing financial interest.

## ACKNOWLEDGMENTS

We are thankful to Julia Zaikina (ISU) for access to the Spark Plasma Sintering instrument, Sarah Gooding and Jake Lepine (SSRL) for help in the fabrication of the *operando* cell for GIXAS measurements, and Anja Schreiber (GFZ) for help with FIB specimen preparation. This research was supported by the National Science Foundation Grant No. 1955456. The work at Ames National Laboratory related to sample preparation and polishing (H.W.O., N.O., G.O.) and computations (P.S.) was supported by the DOE Office of Science, Basic Energy Sciences, Materials Science & Engineering Division. The Ames National Laboratory is operated for the U.S. DOE by Iowa State University under contract #DE-AC02-07CH11358. Use of the Stanford Synchrotron Radiation Lightsource, SLAC National Accelerator Laboratory, is supported by the U.S. Department of Energy, Office of Science, Office of Basic Energy Sciences under Contract No. DE-AC02-76SF00515. Support from Co-ACCESS, part of the SUNCAT Center for Interface Science and Catalysis, was provided by the DOE BES, Chemical Sciences, Geosciences, and Biosciences Division. This work benefited from computational support from NERSC, a DOE Office of Science User Facility, under contract no. DE-AC02-05CH11231. N.S. and Yu.V.K. acknowledge COST Action CA21101 "Confined molecular systems: from a new generation of materials to the stars" (COSY), which is supported by the European Cooperation in Science and Technology. The authors acknowledge support from the European Regional Development Fund and the State of Brandenburg for the Themis Z TEM (part of the Potsdam Imaging and Spectral Analysis (PISA) Facility).

## REFERENCES

(1) Dincer, I.; Acar, C. Review and Evaluation of Hydrogen Production Methods for Better Sustainability. *Int. J. Hydrogen Energy* **2015**, *40* (34), 11094−11111.

(2) Seh, Z. W.; Kibsgaard, J.; Dickens, C. F.; Chorkendorff, I.; Nørskov, J. K.; Jaramillo, T. F. Combining Theory and Experiment in

Electrocatalysis: Insights into Materials Design. *Science* **2017**, *355* (6321), No. eaad4998.
(3) Zeng, M.; Li, Y. Recent Advances in Heterogeneous Electrocatalysts for the Hydrogen Evolution Reaction. *J. Mater. Chem. A* **2015**, *3* (29), 14942−14962.
(4) Subbaraman, R.; Tripkovic, D.; Chang, K.-C.; Strmcnik, D.; Paulikas, A. P.; Hirunsit, P.; Chan, M.; Greeley, J.; Stamenkovic, V.; Markovic, N. M. Trends in Activity for the Water Electrolyser Reactions on 3d M(Ni,Co,Fe,Mn) Hydr(Oxy)Oxide Catalysts. *Nat. Mater.* **2012**, *11* (6), 550−557.
(5) Serov, A.; Kovnir, K.; Shatruk, M.; Kolen'ko, Y. V. Critical Review of Platinum Group Metal-Free Materials for Water Electrolysis: Transition from the Laboratory to the Market: Earth-Abundant Borides and Phosphides as Catalysts for Sustainable Hydrogen Production. *Johnson Matthey Technol. Rev.* **2021**, *65* (2), 207−226.
(6) Feidenhans'l, A. A.; Regmi, Y. N.; Wei, C.; Xia, D.; Kibsgaard, J.; King, L. A. Precious Metal Free Hydrogen Evolution Catalyst Design and Application. *Chem. Rev.* **2024**, *124* (9), 5617−5667.
(7) Li, X.; Wang, H.; Yang, H.; Cai, W.; Liu, S.; Liu, B. In Situ/Operando Characterization Techniques to Probe the Electrochemical Reactions for Energy Conversion. *Small Methods* **2018**, *2* (6), 1700395.
(8) Li, J.; Gong, J. *Operando* Characterization Techniques for Electrocatalysis. *Energy Environ. Sci.* **2020**, *13* (11), 3748−3779.
(9) Fang, L.; Seifert, S.; Winans, R. E.; Li, T. Operando XAS/SAXS: Guiding Design of Single-Atom and Subnanocluster Catalysts. *Small Methods* **2021**, *5* (5), 2001194.
(10) Yang, Y.; Xiong, Y.; Zeng, R.; Lu, X.; Krumov, M.; Huang, X.; Xu, W.; Wang, H.; Di Salvo, F. J.; Brock.; et al. *Operando* Methods in Electrocatalysis. *ACS Catal.* **2021**, *11* (3), 1136−1178.
(11) Wei, X.; Wang, X.; An, Q.; Han, C.; Mai, L. Operando X-ray Diffraction Characterization for Understanding the Intrinsic Electrochemical Mechanism in Rechargeable Battery Materials. *Small Methods* **2017**, *1* (5), 1700083.
(12) Zhu, W.; Liu, D.; Paolella, A.; Gagnon, C.; Gariépy, V.; Vijh, A.; Zaghib, K. Application of Operando X-Ray Diffraction and Raman Spectroscopies in Elucidating the Behavior of Cathode in Lithium-Ion Batteries. *Front. Energy Res.* **2018**, *6*, 66.
(13) Chen, M.; Liu, D.; Qiao, L.; Zhou, P.; Feng, J.; Ng, K. W.; Liu, Q.; Wang, S.; Pan, H. In-Situ/Operando Raman Techniques for in-Depth Understanding on Electrocatalysis. *Chem. Eng. J.* **2023**, *461*, 141939.
(14) AlSalka, Y.; Schwabe, S.; Geweke, J.; Ctistis, G.; Wackerbarth, H. Electrochemical and Photoelectrochemical Water Splitting: Operando Raman and Fourier Transform Infrared Spectroscopy as Useful Probing Techniques. *Energy Technol.* **2023**, *11* (3), 2200788.
(15) Liu, D.; Shadike, Z.; Lin, R.; Qian, K.; Li, H.; Li, K.; Wang, S.; Yu, Q.; Liu, M.; Ganapathy, S.; et al. Review of Recent Development of In Situ/Operando Characterization Techniques for Lithium Battery Research. *Adv. Mater.* **2019**, *31* (28), 1806620.
(16) Benayad, A.; Morales-Ugarte, J. E.; Santini, C. C.; Bouchet, R. Operando XPS: A Novel Approach for Probing the Lithium/Electrolyte Interphase Dynamic Evolution. *J. Phys. Chem. A* **2021**, *125* (4), 1069−1081.
(17) Tyukalova, E.; Vimal Vas, J.; Ignatans, R.; Mueller, A. D.; Medwal, R.; Imamura, M.; Asada, H.; Fukuma, Y.; Rawat, R. S.; Tileli, V.; Duchamp, M. Challenges and Applications to *Operando* and *In Situ* TEM Imaging and Spectroscopic Capabilities in a Cryogenic Temperature Range. *Acc. Chem. Res.* **2021**, *54* (16), 3125−3135.
(18) Feijóo, J.; Yang, Y.; Fonseca Guzman, M. V.; Vargas, A.; Chen, C.; Pollock, C. J.; Yang, P. *Operando* High-Energy-Resolution X-Ray Spectroscopy of Evolving Cu Nanoparticle Electrocatalysts for $CO_2$ Reduction. *J. Am. Chem. Soc.* **2023**, *145* (37), 20208−20213.
(19) Chen, P.-C.; Chen, C.; Yang, Y.; Maulana, A. L.; Jin, J.; Feijoo, J.; Yang, P. Chemical and Structural Evolution of AgCu Catalysts in Electrochemical $CO_2$ Reduction. *J. Am. Chem. Soc.* **2023**, *145* (18), 10116−10125.
(20) Yang, Y.; Louisia, S.; Yu, S.; Jin, J.; Roh, I.; Chen, C.; Fonseca Guzman, M. V.; Feijóo, J.; Chen, P.-C.; Wang, H.; Pollock, C. J.; Huang, X.; Shao, Y.-T.; Wang, C.; Muller, D. A.; Abruña, H. D.; Yang, P. Operando Studies Reveal Active Cu Nanograins for $CO_2$ Electroreduction. *Nature* **2023**, *614*, 262−269.
(21) Zhang, B.; Zheng, X.; Voznyy, O.; Comin, R.; Bajdich, M.; García-Melchor, M.; Han, L.; Xu, J.; Liu, M.; Zheng, L.; García De Arquer, F. P.; Dinh, C. T.; Fan, F.; Yuan, M.; Yassitepe, E.; Chen, N.; Regier, T.; Liu, P.; Li, Y.; De Luna, P.; Janmohamed, A.; Xin, H. L.; Yang, H.; Vojvodic, A.; Sargent, E. H. Homogeneously Dispersed Multimetal Oxygen-Evolving Catalysts. *Science* **2016**, *352*, 333−337.
(22) Zuo, S.; Wu, Z.; Zhang, H.; Lou, X. W.; David. Operando Monitoring and Deciphering the Structural Evolution in Oxygen Evolution Electrocatalysis. *Adv. Energy Mater.* **2022**, *12* (8), 2103383.
(23) Zhao, S.; Tan, C.; He, C.-T.; An, P.; Xie, F.; Jiang, S.; Zhu, Y.; Wu, K.-H.; Zhang, B.; Li, H.; Zhang, J.; Chen, Y.; Liu, S.; Dong, J.; Tang, Z. Structural Transformation of Highly Active Metal−Organic Framework Electrocatalysts during the Oxygen Evolution Reaction. *Nat. Energy* **2020**, *5*, 881−890.
(24) Zhao, Y.; Dongfang, N.; Triana, C. A.; Huang, C.; Erni, R.; Wan, W.; Li, J.; Stoian, D.; Pan, L.; Zhang, P.; Lan, J.; Iannuzzi, M.; Patzke, G. R. Dynamics and Control of Active Sites in Hierarchically Nanostructured Cobalt Phosphide/Chalcogenide-Based Electrocatalysts for Water Splitting. *Energy Environ. Sci.* **2022**, *15* (2), 727−739.
(25) Deng, L.; Hung, S.-F.; Zhao, S.; Zeng, W.-J.; Lin, Z.-Y.; Hu, F.; Xie, Y.; Yin, L.; Li, L.; Peng, S. Unveiling Coordination Transformation for Dynamically Enhanced Hydrogen Evolution Catalysis. *Energy Environ. Sci.* **2023**, *16* (11), 5220−5230.
(26) Huang, J.; Hao, M.; Mao, B.; Zheng, L.; Zhu, J.; Cao, M. The Underlying Molecular Mechanism of Fence Engineering to Break the Activity−Stability Trade-Off in Catalysts for the Hydrogen Evolution Reaction. *Angew. Chem., Int. Ed.* **2022**, *61* (10), No. e202114899.
(27) Cao, L.; Luo, Q.; Liu, W.; Lin, Y.; Liu, X.; Cao, Y.; Zhang, W.; Wu, Y.; Yang, J.; Yao, T.; Wei, S. Identification of Single-Atom Active Sites in Carbon-Based Cobalt Catalysts during Electrocatalytic Hydrogen Evolution. *Nat. Catal.* **2019**, *2* (2), 134−141.
(28) Zhu, Y.; Chen, H.-C.; Hsu, C.-S.; Lin, T.-S.; Chang, C.-J.; Chang, S.-C.; Tsai, L.-D.; Chen, H. M. Operando Unraveling of the Structural and Chemical Stability of P-Substituted $CoSe_2$ Electrocatalysts toward Hydrogen and Oxygen Evolution Reactions in Alkaline Electrolyte. *ACS Energy Lett.* **2019**, *4* (4), 987−994.
(29) Sa, Y. J.; Park, S. O.; Jung, G. Y.; Shin, T. J.; Jeong, H. Y.; Kwak, S. K.; Joo, S. H. Heterogeneous Co−N/C Electrocatalysts with Controlled Cobalt Site Densities for the Hydrogen Evolution Reaction: Structure−Activity Correlations and Kinetic Insights. *ACS Catal.* **2019**, *9* (1), 83−97.
(30) Owens-Baird, B.; Kolen'ko, Y. V.; Kovnir, K. Structure−Activity Relationships for Pt-Free Metal Phosphide Hydrogen Evolution Electrocatalysts. *Chem. Eur. J.* **2018**, *24* (29), 7298−7311.
(31) Liu, P.; Rodriguez, J. A.; Asakura, T.; Gomes, J.; Nakamura, K. Desulfurization Reactions on $Ni_2P(001)$ and $\alpha$-$Mo_2C(001)$ Surfaces: Complex Role of P and C Sites. *J. Phys. Chem. B* **2005**, *109* (10), 4575−4583.
(32) Liu, P.; Rodriguez, J. A. Catalysts for Hydrogen Evolution from the [NiFe] Hydrogenase to the $Ni_2P(001)$ Surface: The Importance of Ensemble Effect. *J. Am. Chem. Soc.* **2005**, *127* (42), 14871−14878.
(33) Laursen, A. B.; Wexler, R. B.; Whitaker, M. J.; Izett, E. J.; Calvinho, K. U. D.; Hwang, S.; Rucker, R.; Wang, H.; Li, J.; Garfunkel, E.; Greenblatt, M.; Rappe, A. M.; Dismukes, G. C. Climbing the Volcano of Electrocatalytic Activity While Avoiding Catalyst Corrosion: $Ni_3P$, a Hydrogen Evolution Electrocatalyst Stable in Both Acid and Alkali. *ACS Catal.* **2018**, *8* (5), 4408−4419.
(34) Partanen, L.; Hakala, M.; Laasonen, K. Hydrogen Adsorption Trends on Various Metal-Doped $Ni_2P$ Surfaces for Optimal Catalyst Design. *Phys. Chem. Chem. Phys.* **2019**, *21* (1), 184−191.
(35) Wexler, R. B.; Martirez, J. M. P.; Rappe, A. M. Active Role of Phosphorus in the Hydrogen Evolving Activity of Nickel Phosphide (0001) Surfaces. *ACS Catal.* **2017**, *7* (11), 7718−7725.


https://doi.org/10.1021/jacs.6c01756
J. Am. Chem. Soc. 2026, 148, 10241−10256

(36) Kong, S.; Singh, P.; Akopov, G.; Jing, D.; Davis, R.; Perez-Aguilar, J.; Hong, J.; Lee, S. J.; Viswanathan, G.; Soto, E.; Azhan, M.; Fernandes, T.; Harycki, S.; Gundlach-Graham, A.; Kolen'ko, Y. V.; Johnson, D. D.; Kovnir, K. Probing of the Noninnocent Role of P in Transition-Metal Phosphide Hydrogen Evolution Reaction Electrocatalysts via Replacement with Electropositive Si. *Chem. Mater.* **2023**, *35* (14), 5300−5310.
(37) Saadi, F. H.; Carim, A. I.; Drisdell, W. S.; Gul, S.; Baricuatro, J. H.; Yano, J.; Soriaga, M. P.; Lewis, N. S. *Operando* Spectroscopic Analysis of CoP Films Electrocatalyzing the Hydrogen-Evolution Reaction. *J. Am. Chem. Soc.* **2017**, *139* (37), 12927−12930.
(38) Thersleff, T.; Budnyk, S.; Drangai, L.; Slabon, A. Dissecting Complex Nanoparticle Heterostructures via Multimodal Data Fusion with Aberration-Corrected STEM Spectroscopy. *Ultramicroscopy* **2020**, *219*, 113116.
(39) Pattengale, B.; Huang, Y.; Yan, X.; Yang, S.; Younan, S.; Hu, W.; Li, Z.; Lee, S.; Pan, X.; Gu, J.; et al. Dynamic Evolution and Reversibility of Single-Atom Ni(II) Active Site in 1T-$MoS_2$ Electrocatalysts for Hydrogen Evolution. *Nat. Commun.* **2020**, *11* (1), 4114.
(40) Staszak-Jirkovský, J.; Malliakas, C. D.; Lopes, P. P.; Danilovic, N.; Kota, S. S.; Chang, K.-C.; Genorio, B.; Strmcnik, D.; Stamenkovic, V. R.; Kanatzidis, M. G.; Markovic, N. M. Design of Active and Stable Co−Mo−$S_x$ Chalcogels as pH-Universal Catalysts for the Hydrogen Evolution Reaction. *Nat. Mater.* **2016**, *15* (2), 197−203.
(41) Wang, M.; Árnadóttir, L.; Xu, Z. J.; Feng, Z. In Situ X-Ray Absorption Spectroscopy Studies of Nanoscale Electrocatalysts. *Nano Micro Lett.* **2019**, *11* (1), 47.
(42) Lin, S.-C.; Chang, C.-C.; Chiu, S.-Y.; Pai, H.-T.; Liao, T.-Y.; Hsu, C.-S.; Chiang, W.-H.; Tsai, M.-K.; Chen, H. M. Operando Time-Resolved X-Ray Absorption Spectroscopy Reveals the Chemical Nature Enabling Highly Selective $CO_2$ Reduction. *Nat. Commun.* **2020**, *11* (1), 3525.
(43) Li, J.; Banis, M. N.; Ren, Z.; Adair, K. R.; Doyle-Davis, K.; Meira, D. M.; Finfrock, Y. Z.; Zhang, L.; Kong, F.; Sham, T.; et al. Unveiling the Nature of Pt Single-Atom Catalyst during Electrocatalytic Hydrogen Evolution and Oxygen Reduction Reactions. *Small* **2021**, *17* (11), 2007245.
(44) Fang, S.; Zhu, X.; Liu, X.; Gu, J.; Liu, W.; Wang, D.; Zhang, W.; Lin, Y.; Lu, J.; Wei, S.; et al. Uncovering Near-Free Platinum Single-Atom Dynamics during Electrochemical Hydrogen Evolution Reaction. *Nat. Commun.* **2020**, *11* (1), 1029.
(45) Farmand, M.; Landers, A. T.; Lin, J. C.; Feaster, J. T.; Beeman, J. W.; Ye, Y.; Clark, E. L.; Higgins, D.; Yano, J.; Davis, R. C.; Mehta, A.; Jaramillo, T. F.; Hahn, C.; Drisdell, W. S. Electrochemical Flow Cell Enabling *Operando* Probing of Electrocatalyst Surfaces by X-Ray Spectroscopy and Diffraction. *Phys. Chem. Chem. Phys.* **2019**, *21* (10), 5402−5408.
(46) Lee, S. H.; Lin, J. C.; Farmand, M.; Landers, A. T.; Feaster, J. T.; Avilés Acosta, J. E.; Beeman, J. W.; Ye, Y.; Yano, J.; Mehta, A.; Davis, R. C.; Jaramillo, T. F.; Hahn, C.; Drisdell, W. S. Oxidation State and Surface Reconstruction of Cu under $CO_2$ Reduction Conditions from *In Situ* X-Ray Characterization. *J. Am. Chem. Soc.* **2021**, *143* (2), 588−592.
(47) Ravel, B.; Newville, M. *ATHENA*, *ARTEMIS*, *HEPHAESTUS*: Data Analysis for X-Ray Absorption Spectroscopy Using *IFEFFIT*. *J. Synchrotron Radiat.* **2005**, *12* (4), 537−541.
(48) Hafner, J. *Ab-Initio* Simulations of Materials Using VASP: Density-Functional Theory and Beyond. *J. Comput. Chem.* **2008**, *29* (13), 2044−2078.
(49) Kresse, G.; Hafner, J. Norm-Conserving and Ultrasoft Pseudopotentials for First-Row and Transition Elements. *J. Phys.: Condens. Matter* **1994**, *6* (40), 8245−8257.
(50) Perdew, J. P.; Burke, K.; Ernzerhof, M. Generalized Gradient Approximation Made Simple. *Phys. Rev. Lett.* **1996**, *77* (18), 3865−3868.
(51) Monkhorst, H. J.; Pack, J. D. Special Points for Brillouin-Zone Integrations. *Phys. Rev. B* **1976**, *13* (12), 5188−5192.
(52) Singh, P.; Harbola, M. K.; Sanyal, B.; Mookerjee, A. Accurate Determination of Band Gaps within Density Functional Formalism. *Phys. Rev. B* **2013**, *87* (23), 235110.
(53) Söderlind, P.; Turchi, P. E. A.; Landa, A.; Lordi, V. Ground-State Properties of Rare-Earth Metals: An Evaluation of Density-Functional Theory. *J. Phys.: Condens. Matter* **2014**, *26* (41), 416001.
(54) Zagorac, D.; Müller, H.; Ruehl, S.; Zagorac, J.; Rehme, S. Recent Developments in the Inorganic Crystal Structure Database: Theoretical Crystal Structure Data and Related Features. *J. Appl. Crystallogr.* **2019**, *52* (5), 918−925.
(55) Giese, T. J.; York, D. M. A GPU-Accelerated Parameter Interpolation Thermodynamic Integration Free Energy Method. *J. Chem. Theory Comput.* **2018**, *14* (3), 1564−1582.
(56) Wang, V.; Xu, N.; Liu, J.-C.; Tang, G.; Geng, W.-T. VASPKIT: A User-Friendly Interface Facilitating High-Throughput Computing and Analysis Using VASP Code. *Comput. Phys. Commun.* **2021**, *267*, 108033.
(57) Tian, X.; Wang, T.; Fan, L.; Wang, Y.; Lu, H.; Mu, Y. A DFT Based Method for Calculating the Surface Energies of Asymmetric MoP Facets. *Appl. Surf. Sci.* **2018**, *427*, 357−362.
(58) Kong, S.; Raturi, D.; Owens-Baird, B.; Zheng, W.; Kolen'ko, Y.; Singh, P.; Johnson, D. D.; Kovnir, K. Facet-Dependent Hydrogen Evolution Reaction on $M_2P$ (M = Ni, Co, Fe) Single Crystals. *ACS Catal.* **2025**, *15*, 18723−18737.
(59) Rauri, D.. *Realizing Platinum-free catalysts for hydrogen production through modular, reliable, and efficient models of surfaces and chemical disorder*. Ph.D. Dissertation; Lowa State University, 2025.
(60) Kas, J. J.; Sorini, A. P.; Prange, M. P.; Cambell, L. W.; Soininen, J. A.; Rehr, J. J. Many-Pole Model of Inelastic Losses in x-Ray Absorption Spectra. *Phys. Rev. B* **2007**, *76* (19), 195116.
(61) Hu, J.; Zheng, S.; Zhao, X.; Yao, X.; Chen, Z. A theoretical study on the surface and interfacial properties of $Ni_3P$ for the hydrogen evolution reaction. *J. Mater. Chem. A* **2018**, *6*, 7827−7834.
(62) Banerjee, S.; Kakekhani, A.; Wexler, R. B.; Rappe, A. M. Relationship between the Surface Reconstruction of Nickel Phosphides and Their Activity toward the Hydrogen Evolution Reaction. *ACS Catal.* **2023**, *13*, 4611−4621.
(63) Wexler, R. B.; Martirez, J. M. P.; Rappe, A. M. Stable Phosphorus-Enriched (0001) Surfaces of Nickel Phosphides. *Chem. Mater.* **2016**, *28*, 5365−5372.
(64) Moon, J.-S.; Jang, J.-H.; Kim, E.-G.; Chung, Y.-H.; Yoo, S. J.; Lee, Y.-K. The nature of active sites of $Ni_2P$ electrocatalyst for hydrogen evolution reaction. *J. Catal.* **2015**, *326*, 92−99.
(65) Wexler, R. B.; Martirez, J. M. P.; Rappe, A. M. Chemical Pressure-Driven Enhancement of the Hydrogen Evolving Activity of $Ni_2P$ from Nonmetal Surface Doping Interpreted via Machine Learning. *J. Am. Chem. Soc.* **2018**, *140*, 4678−4683.
(66) Wang, J.; Gao, Y.; Kong, H.; Kim, J.; Choi, S.; Ciucci, F.; Hao, Y.; Yang, S.; Shao, Z.; Lim, J. Non-precious-metal catalysts for alkaline water electrolysis: operando characterizations, theoretical calculations, and recent advances. *Chem. Soc. Rev.* **2020**, *49*, 9154−9196.
(67) Fu, C.; Feng, L.; Yin, H.; Li, Y.; Xie, Y.; Feng, Y.; Zhao, Y.; Cao, L.; Huang, J.; Liu, Y. Heterogeneous $Ni_3P$/Ni nanoparticles with optimized Ni active sites anchored in N-doped mesoporous nanofibers for boosting pH-universal hydrogen evolution. *Nanoscale* **2022**, *14*, 14779−14788.
(68) Jin, L.; Xia, H.; Huang, Z.; Lv, C.; Wang, J.; Humphrey, M. G.; Zhang, C. Phase separation synthesis of trinickel monophosphide porous hollow nanospheres for efficient hydrogen evolution. *J. Mater. Chem. A* **2016**, *4*, 10925−10932.
(69) Kucernak, A. R. J.; Sundaram, V. N. N. Nickel Phosphide: The Effect of Phosphorus Content on Hydrogen Evolution Activity and Corrosion Resistance in Acidic Medium. *J. Mater. Chem. A* **2014**, *2* (41), 17435−17445.
(70) Uvarov, A. V.; Gudovskikh, A. S. Optical Emission Spectroscopy of Gallium Phosphide Plasma-Enhanced Atomic Layer Deposition. *J. Phys.: Conf. Ser.* **2018**, *1038*, 012108.


https://doi.org/10.1021/jacs.6c01756
J. Am. Chem. Soc. 2026, 148, 10241−10256

(71) Zhang, H.; Hagen, D. J.; Li, X.; Graff, A.; Heyroth, F.; Fuhrmann, B.; Kostanovskiy, I.; Schweizer, S. L.; Caddeo, F.; Maijenburg, A. W.; Parkin, S.; Wehrspohn, R. B. Atomic Layer Deposition of Cobalt Phosphide for Efficient Water Splitting. *Angew. Chem., Int. Ed.* **2020**, *59* (39), 17172−17176.
(72) Quadir, S.; Yuan, Z.; Esparza, G. L.; Dugu, S.; Mangum, J. S.; Pike, A.; Hasan, M. R.; Kassa, G.; Wang, X.; Coban, Y.; et al. Low-Temperature Synthesis of Stable $CaZn_2P_2$ Zintl Phosphide Thin Films as Candidate Top Absorbers. *Adv. Energy Mater.* **2024**, *14*, 2402640.
(73) Hellstern, T. R.; Benck, J. D.; Kibsgaard, J.; Hahn, C.; Jaramillo, T. F. Engineering Cobalt Phosphide (CoP) Thin Film Catalysts for Enhanced Hydrogen Evolution Activity on Silicon Photocathodes. *Adv. Energy Mater.* **2016**, *6* (4), 1501758.
(74) Rongé, J.; Dobbelaere, T.; Henderick, L.; Minjauw, M. M.; Sree, S. P.; Dendooven, J.; Martens, J. A.; Detavernier, C. Bifunctional Earth-Abundant Phosphate/Phosphide Catalysts Prepared *via* Atomic Layer Deposition for Electrocatalytic Water Splitting. *Nanoscale Adv.* **2019**, *1* (10), 4166−4172.
(75) Trevorah, R. M.; Chantler, C. T.; Schalken, M. J. Solving Self-Absorption in Fluorescence. *IUCrJ* **2019**, *6* (4), 586−602.
(76) Colpas, G. J.; Maroney, M. J.; Bagyinka, C.; Kumar, M.; Willis, W. S.; Suib, S. L.; Mascharak, P. K.; Baidya, N. X-Ray Spectroscopic Studies of Nickel Complexes, with Application to the Structure of Nickel Sites in Hydrogenases. *Inorg. Chem.* **1991**, *30* (5), 920−928.
(77) Liu, E.; Li, J.; Jiao, L.; Doan, H. T. T.; Liu, Z.; Zhao, Z.; Huang, Y.; Abraham, K. M.; Mukerjee, S.; Jia, Q. Unifying the Hydrogen Evolution and Oxidation Reactions Kinetics in Base by Identifying the Catalytic Roles of Hydroxyl-Water-Cation Adducts. *J. Am. Chem. Soc.* **2019**, *141* (7), 3232−3239.
(78) Ding, X.; Liu, D.; Zhao, P.; Chen, X.; Wang, H.; Oropeza, F. E.; Gorni, G.; Barawi, M.; García-Tecedor, M.; De La Peña O'Shea, V. A.; et al. Dynamic Restructuring of Nickel Sulfides for Electrocatalytic Hydrogen Evolution Reaction. *Nat. Commun.* **2024**, *15* (1), 5336.
(79) Hersbach, T. J. P.; Garcia-Esparza, A. T.; Hanselman, S.; Paredes Mellone, O. A.; Hoogenboom, T.; McCrum, I. T.; Anastasiadou, D.; Feaster, J. T.; Jaramillo, T. F.; Vinson, J.; Kroll, T.; Garcia, A. C.; Krtil, P.; Sokaras, D.; Koper, M. T. M. Platinum Hydride Formation during Cathodic Corrosion in Aqueous Solutions. *Nat. Mater.* **2025**, *24* (4), 574−580.
(80) Pandya, K. I.; Hoffman, R. W.; McBreen, J.; O'Grady, W. E. In Situ X-Ray Absorption Spectroscopic Studies of Nickel Oxide Electrodes. *J. Electrochem. Soc.* **1990**, *137* (2), 383−388.
(81) Luo, Y.; Zhang, Z.; Yang, F.; Li, J.; Liu, Z.; Ren, W.; Zhang, S.; Liu, B. Stabilized Hydroxide-Mediated Nickel-Based Electrocatalysts for High-Current-Density Hydrogen Evolution in Alkaline Media. *Energy Environ. Sci.* **2021**, *14* (8), 4610−4619.
(82) Franke, R. X-Ray Absorption and Photoelectron Spectroscopy Investigation of Binary Nickel Phosphides. *Spectrochim. Acta, Part A* **1997**, *53* (7), 933−941.
(83) Lee, K.; Wei, H.; Blake, A. V.; Donahue, C. M.; Keith, J. M.; Daly, S. R. Measurement of Diphosphine $\sigma$-Donor and $\pi$-Acceptor Properties in $d^0$ Titanium Complexes Using Ligand K-Edge XAS and TDDFT. *Inorg. Chem.* **2018**, *57* (16), 10277−10286.
(84) Dey, A.; Okamura, T.; Ueyama, N.; Hedman, B.; Hodgson, K. O.; Solomon, E. I. Sulfur K-Edge XAS and DFT Calculations on P450 Model Complexes: Effects of Hydrogen Bonding on Electronic Structure and Redox Potentials. *J. Am. Chem. Soc.* **2005**, *127* (34), 12046−12053.
(85) Owens-Baird, B.; Sousa, J. P. S.; Ziouani, Y.; Petrovykh, D. Y.; Zarkevich, N. A.; Johnson, D. D.; Kolen'ko, Y. V.; Kovnir, K. Crystallographic Facet Selective HER Catalysis: Exemplified in FeP and $NiP_2$ Single Crystals. *Chem. Sci.* **2020**, *11* (19), 5007−5016.
(86) Fu, Q.; Wang, X.; Han, J.; Zhong, J.; Zhang, T.; Yao, T.; Xu, C.; Gao, T.; Xi, S.; Liang, C.; Xu, L.; Xu, P.; Song, B. Phase-Junction Electrocatalysts towards Enhanced Hydrogen Evolution Reaction in Alkaline Media. *Angew. Chem., Int. Ed.* **2021**, *60* (1), 259−267.
(87) Zhao, X.; Zhang, Z.; Cao, X.; Hu, J.; Wu, X.; Ng, A. Y. R.; Lu, G.-P.; Chen, Z. Elucidating the Sources of Activity and Stability of FeP Electrocatalyst for Hydrogen Evolution Reactions in Acidic and Alkaline Media. *Appl. Catal. B Environ.* **2020**, *260*, 118156.




https://doi.org/10.1021/jacs.6c01756
J. Am. Chem. Soc. 2026, 148, 10241−10256